

AEDC-TR-69-213

241  
**ARCHIVE COPY  
DO NOT LOAN**



# **DETERMINATION OF HEMISPHERICAL EMITTANCE BY MEASUREMENTS OF INFRARED BI-HEMISPHERICAL REFLECTANCE**

**Fred G. Sherrell**

**ARO, Inc.**

**November 1969**

This document has been approved for public release  
and sale; its distribution is unlimited.

**AEROSPACE ENVIRONMENTAL FACILITY  
ARNOLD ENGINEERING DEVELOPMENT CENTER  
AIR FORCE SYSTEMS COMMAND  
ARNOLD AIR FORCE STATION, TENNESSEE**

AEDC TECHNICAL LIBRARY



5 0720 00032 0749

DEPT OF DEFENSE  
AIR FORCE  
501000-01-0001

# ***NOTICES***

When U. S. Government drawings, specifications, or other data are used for any purpose other than a definitely related Government procurement operation, the Government thereby incurs no responsibility nor any obligation whatsoever, and the fact that the Government may have formulated, furnished, or in any way supplied the said drawings, specifications, or other data, is not to be regarded by implication or otherwise, or in any manner licensing the holder or any other person or corporation, or conveying any rights or permission to manufacture, use, or sell any patented invention that may in any way be related thereto.

Qualified users may obtain copies of this report from the Defense Documentation Center.

References to named commercial products in this report are not to be considered in any sense as an endorsement of the product by the United States Air Force or the Government.

DETERMINATION OF HEMISPHERICAL EMITTANCE BY  
MEASUREMENTS OF INFRARED BI-HEMISPHERICAL  
REFLECTANCE

Fred G. Sherrell  
ARO, Inc.

This document has been approved for public release  
and sale; its distribution is unlimited.

## FOREWORD

The research reported herein was sponsored by Headquarters, Arnold Engineering Development Center (AEDC), Air Force Systems Command (AFSC), Arnold Air Force Station, Tennessee, under Program Elements 35119F and 35121F.

The research was conducted and reported by ARO, Inc. (a subsidiary of Sverdrup & Parcel and Associates, Inc.) contract operator of AEDC, AFSC, under Contract F40600-69-C-0001. The research was performed in the period from January 1968 to June 1969. The direct costs were approximately equally distributed among ARO Projects SB0721, SM0718, and ST8002. The manuscript was submitted for publication on September 2, 1969.

The work reported herein was used by the author as a thesis for partial fulfillment of the requirements for the degree of master of science from The University of Tennessee Space Institute.

This technical report has been reviewed and approved.

Robert T. Otto  
Major, USAF  
AF Representative, AEF  
Directorate of Test

Roy R. Croy, Jr.  
Colonel, USAF  
Director of Test

## ABSTRACT

A technique for the experimental determination of spectral, hemispherical emittance of surfaces in the infrared wavelength region is suggested. The technique consists of using an infrared integrating sphere to measure spectral, bi-hemispherical reflectance. The feasibility of the technique is justified both on an analytical basis and, to the extent possible, on an experimental basis. A spectral, bi-hemispherical reflectometer is described. The device produces reflectance measurements with an estimated uncertainty of  $\pm 2$  per cent of full scale at 5 microns. Due to detector noise the estimated uncertainty increases to  $\pm 10$  per cent of full scale at 16 microns. Reflectometer measurements of the spectral hemispherical emittance of fused quartz in the 5 to 16 micron range are presented to illustrate operation of the reflectometer. It is concluded that the device has high potential as an analytical instrument and that developmental efforts should be directed toward extending its wavelength range.

## TABLE OF CONTENTS

CHAPTER	PAGE
I. INTRODUCTION . . . . .	1
II. ANALYSIS . . . . .	11
Analysis of a Technique for Measuring Bi-	
Hemispherical Reflectance with an	
Integrating Sphere . . . . .	11
Calculation of $(\Delta E/E)$ . . . . .	17
III. INFRARED REFLECTOMETER DESIGN . . . . .	23
Description of an Infrared Bi-Hemispherical	
Reflectometer . . . . .	23
Significant Design Problems . . . . .	32
IV. EXPERIMENTAL RESULTS . . . . .	46
Summary and Analysis of Experimental Results . .	46
Error Sources . . . . .	53
V. CONCLUSIONS . . . . .	60
BIBLIOGRAPHY . . . . .	61
APPENDIXES . . . . .	63
A. RELATIONSHIP OF DIRECTIONAL EMITTANCE TO	
HEMISPHERICAL EMITTANCE . . . . .	65
B. SHAPE FACTOR FOR ENERGY TRANSFER BETWEEN TWO	
AREAS ON A SPHERICAL SURFACE . . . . .	68

## LIST OF FIGURES

FIGURE	PAGE
1. Apparatus for Hemispherical-Emittance Determinations . . . . .	4
2. Total Emittance Calorimeter . . . . .	6
3. Schematic of Directional Reflectance Apparatus . .	8
4. Integrating Sphere and Associated Components for Bi-Hemispherical Reflectance Measurements . . . .	13
5. Inter-Reflection Components . . . . .	18
6. Power Retained in Inter-Reflection Components . . .	19
7. Infrared Bi-Hemispherical Reflectometer Schematic . . . . .	24
8. Infrared Bi-Hemispherical Reflectometer Photograph . . . . .	25
9. Details of Interior of Infrared Integrating Sphere . . . . .	26
10. Block Diagram of the Infrared Detection and Slit Control Instrumentation . . . . .	29
11. Example of Reflectometer Data for a Gold Mirror, a Sand Blasted Aluminum Surface and a Second Surface Quartz Mirror . . . . .	33
12. Diffuse Component of Hemispherical-Directional Reflectance in the Normal Direction ( $\theta = 0^\circ$ ) at $10\mu$ for Gold Coated Silicon Carbide Abrasive Papers of Varying Grit Sizes . . . . .	35

FIGURE	PAGE
13. Theoretical, Normalized Distributions of $10\mu$ Energy Reflected from Directionally Illuminated Samples . . . . .	36
14. Directional Sensitivity of a Thermistor Detector with Flat KRS-5 Window . . . . .	38
15. Directional Sensitivity of a Thermistor Detector with Hemispherical KRS-5 Dome . . . . .	41
16. Normalized Power Density Spectrum of the Electrical Noise from a Thermistor Infrared Detector Compared to a ( $1/f^{1.5}$ ) Spectral Variation . . . . .	44
17. Plot of Fractional Change in Hemispherical Detector Signal Versus Bi-Hemispherical Reflectance at $7\mu$ . . . . .	48
18. Spectral Hemispherical Emittance of Fused Quartz .	54
19. Spectral Power Emitted from $100^\circ\text{C}$ Fused Quartz .	55
20. Comparison of Detector Signal Levels to Detector Noise at Various Integration Times . . . . .	58
21. Geometry for Shape Factor Definition . . . . .	68
22. Geometrical Relationships when $dA_1$ and $dA_2$ Are Located on a Sphere Wall . . . . .	69



## NOMENCLATURE

$A$	Geometric sphere area less total area of sphere ports
$A_c$	Surface area of calorimetric specimen
$A_d$	Area of hemispherical detector
$A_o$	Geometric area of sphere
$A_s$	Area of test sample
$\Delta B$	Amplifier bandwidth when operating as a lock-in amplifier
$c$	Specific heat of specimen
$c_o$	Speed of light in vacuum
$e_{b\lambda}(T)$	Planck's law for blackbody emissive power per unit area and wavelength at absolute temperature $T$
$e_m(t)$	Product of $e_s(t)$ and $e_r(t)$
$e_n(f)$	The rms detector noise voltage as a function of frequency
$e_r(t)$	Fundamental component of reference signal
$e_s(t)$	Fundamental component of hemispherical detector signal
$e(T)$	Total emissive power per unit area from a surface at temperature $T$
$E$	Hemispherical detector reading with sample port open
$\Delta E$	Change in hemispherical detector reading when a sample is placed on the sample port

$E_n$	Peak-to-peak noise signal ( $\mu\text{v}$ ) from hemispherical detector
$E_s(t)$	Peak voltage of fundamental component of hemispherical detector signal
$f$	Frequency in Hz
$\Delta f$	Amplifier bandwidth when operating as a tuned frequency voltmeter
$g$	Gold
$G$	Amplification gain factor
$h$	Planck's constant
$k$	Boltzmann's constant
$K$	Proportionality constant
$K_1, K_2, K_3$	Proportionality constants
$\text{LN}_2$	Liquid nitrogen
$m$	Mass of specimen
$n$	Index of refraction of medium bounding the infrared emitting surface
$N$	Number of times a specific power component has been reflected from the test sample
$P_o$	Sphere input power at arbitrary wavelength
$r$	Sphere radius
$R$	Equals $2r \cos \theta$
$s$	Sample
$t$	Time
$T$	Absolute temperature
$T_r$	Amplifier rise time (10 to 90 per cent)
$T_w$	Absolute temperature of wall

$v$	Voltage
$\alpha_{\lambda}$	Spectral absorptance of hemispherically illuminated sample
$\alpha_{\lambda}(\theta, \phi)$	Spectral, directional absorptance of a test sample
$\epsilon$	Total hemispherical emittance of a test sample
$\epsilon_n$	Total normal emittance
$\epsilon_{\lambda}$	Spectral hemispherical emittance of a test sample
$(\epsilon_{\lambda})_n$	Normal, spectral emittance of a test sample
$\epsilon_{\lambda}(\theta, \phi)$	Spectral, directional emittance of a test sample
$\theta$	Angle between the normal to a sample surface and the direction of the incident, reflected or emitted radiation
$\lambda$	Wavelength of infrared radiation
$\mu$	Micron ( $10^{-6}$ meter)
$\mu v$	Microvolts
$\rho_s$	Bi-hemispherical sample reflectance of a test sample at an arbitrary wavelength
$\rho_w$	Reflectance of sphere wall coating
$\rho_{\lambda}$	Spectral, bi-hemispherical reflectance of a test sample
$\rho_{\lambda dh}(\theta, \phi)$	Spectral directional-hemispherical reflectance of a test sample
$\rho_{dh}(\theta, \phi)$	Directional-hemispherical reflectance of a test sample at an arbitrary wavelength
$\sigma$	Stefan-Boltzman constant

$\phi$	Azimuthal angle on a test sample surface
$\omega$	Angular frequency in radians/second
$d\omega$	Elemental solid angle

## CHAPTER I

## INTRODUCTION

Many problems, including space simulation and space systems testing, deal with radiative heat transfer from surfaces. Such problems require knowledge of the total hemispherical emittance,  $\epsilon$ , of room temperature surfaces for computations of radiant interchange. An ideal black surface at temperature  $T$ , having an  $\epsilon = 1$ , emits spectral power per unit area and wavelength as determined by Planck's law (1)<sup>1</sup>:

$$e_{b\lambda}(T) = \frac{2\pi hc_o^2}{n^2 \lambda^5 [\exp(hc_o/n\lambda kT) - 1]} \quad (1)$$

The total emitted power per unit area of black surface is found by integrating Planck's law:

$$e_b(T) = \int_0^{\infty} e_{b\lambda}(T) d\lambda \quad (2)$$

The result is the Stefan-Boltzmann law:

$$e_b(T) = n^2 \sigma T^4 \quad (3)$$

The efficiency of a real surface as a power emitter may be specified in terms of the spectral hemispherical emittance,  $\epsilon_\lambda$ , of the surface. The  $\epsilon_\lambda$  is defined as the

---

<sup>1</sup>Numbers in parentheses refer to similarly numbered references in the bibliography.

ratio of the spectral emissive power of wavelength  $\lambda$  from the surface to the spectral emissive power of the same wavelength from an ideal black surface. The total emitted power per unit area of real surface is given by

$$e(T) = \int_0^{\infty} \epsilon_{\lambda} e_{b\lambda}(T) d\lambda \quad (4)$$

The total hemispherical emittance  $\epsilon$  of a surface is defined as the ratio of the emissive power from the surface to the emissive power from an ideal black surface of the same temperature:

$$\epsilon = \frac{\int_0^{\infty} \epsilon_{\lambda} e_{b\lambda}(T) d\lambda}{\int_0^{\infty} e_{b\lambda}(T) d\lambda} \quad (5)$$

If the surface is a "gray" surface, then  $\epsilon_{\lambda}$  is a constant and  $\epsilon = \epsilon_{\lambda}$ . In the general case the surface is non-gray; (i.e.,  $\epsilon_{\lambda}$  varies with  $\lambda$  and  $\epsilon$  varies with surface temperature according to Equation 5).

Regardless of whether the surface is gray or non-gray, there are only three practical approaches to the determination of  $\epsilon$  for near ambient, or below ambient, temperature surfaces:

1. Calorimetric techniques.
2. Measurements of surface emissive power using

cryogenically cooled thermopile detectors.

3. Measurements of infrared reflectance from which, by Kirchhoff's law,  $\epsilon$  can be determined.

The basic type of apparatus employed in calorimetric techniques is illustrated in Figure 1 and described in Reference (2). The sample is suspended by small thermocouple wires in vacuum, and the copper can is immersed in boiling water until the sample reaches about 90 °C. The boiling water is removed, the LN<sub>2</sub> Dewar is raised and the can is quickly cooled to LN<sub>2</sub> temperature. The cooling rate of the specimen is measured and used to calculate  $\epsilon$  at any desired temperature from about 80 °C to about -100 °C. The emittance is calculated from the expression

$$\epsilon = \frac{-mc (dT/dt)}{A_c \sigma (T^4 - T_w^4)} \quad (6)$$

The significant problems which limit the range of applicability of this method are:

1. The sample must be heated in vacuum. This may change the properties of the sample.
2. The specific heat of the sample must be known accurately.
3. An accurate surface temperature measurement must be made.
4. The use of a cryogenic fluid is required.

The calorimetric method is most applicable to metallic samples.

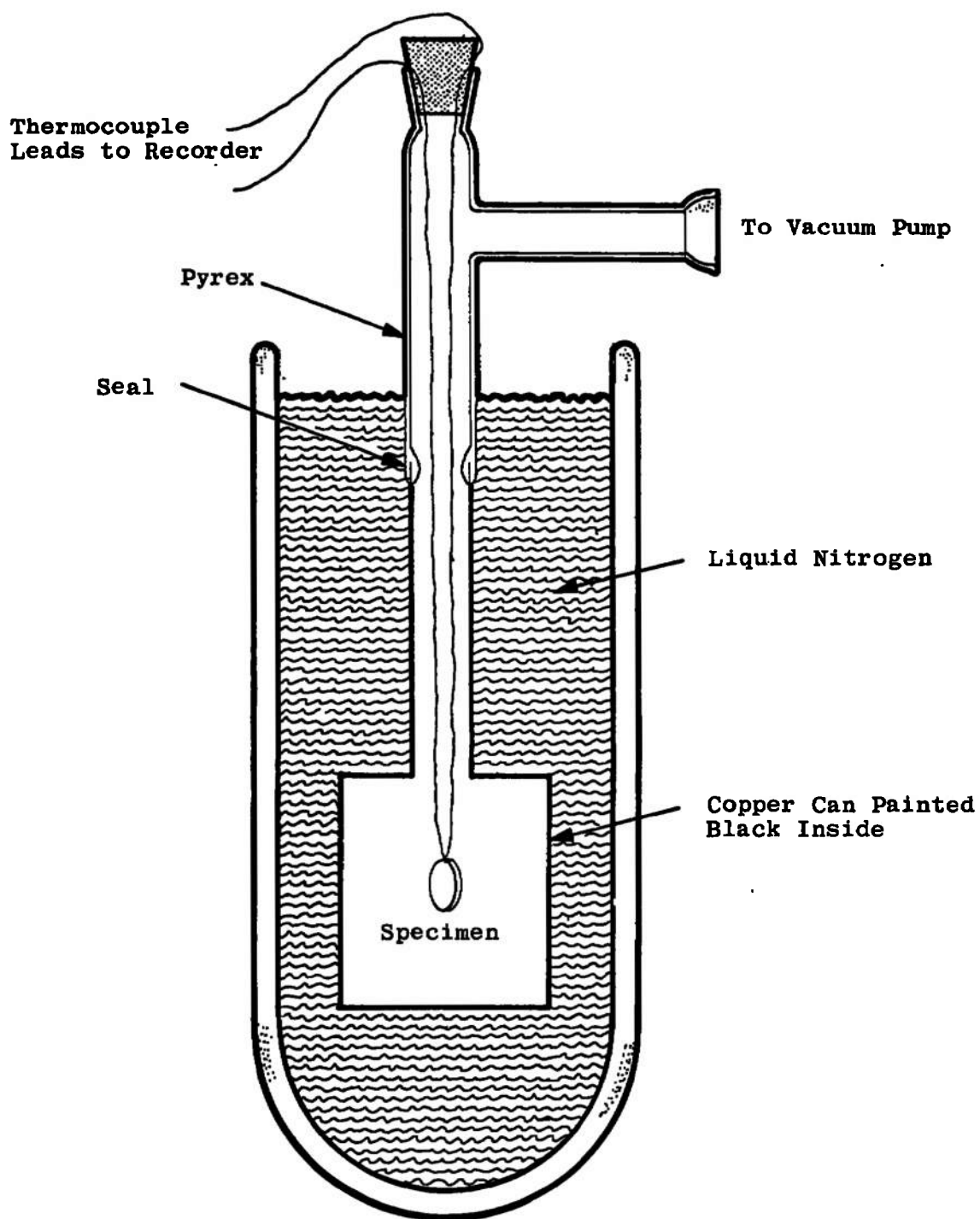


Figure 1. Apparatus for hemispherical-emittance determinations.



The second possible approach to the determination of  $\epsilon$  for ambient temperature surfaces requires the use of a cryogenically cooled thermopile to measure the infrared power emitted into hemispherical space per unit area of surface. Figure 2 shows an example of an emissometer of this type, Reference (3). The apparatus consists of an evacuated,  $\text{LN}_2$ -cooled chamber, a  $\text{LN}_2$ -cooled thermopile and a heated sample holder. The collimating tube between the sample and thermopile is polished copper with a reflectance in the infrared of about 98 per cent. Consequently, the shape factor for transfer of energy from sample to thermopile is very close to unity, and a hemispherical emissive power measurement is assured. The thermopile is calibrated against blackbody radiation by removing the sample holder and installing a heated, blackened cavity over the thermopile.

This type of emissometer is generally applicable to various types of samples with temperatures ranging from  $-100^\circ\text{F}$  to  $+200^\circ\text{F}$ . The most significant problems encountered in its application are:

1. An accurate measurement of surface temperature is required. This may be a significant problem when working with dielectrics.
2. The sample must be installed in a vacuum chamber.
3. The use of a cryogenic fluid is required.

This type of emissometer has a reported maximum measurement uncertainty of  $\pm 3.25$  per cent of magnitude.

The third possible way to determine  $\epsilon$  is to measure

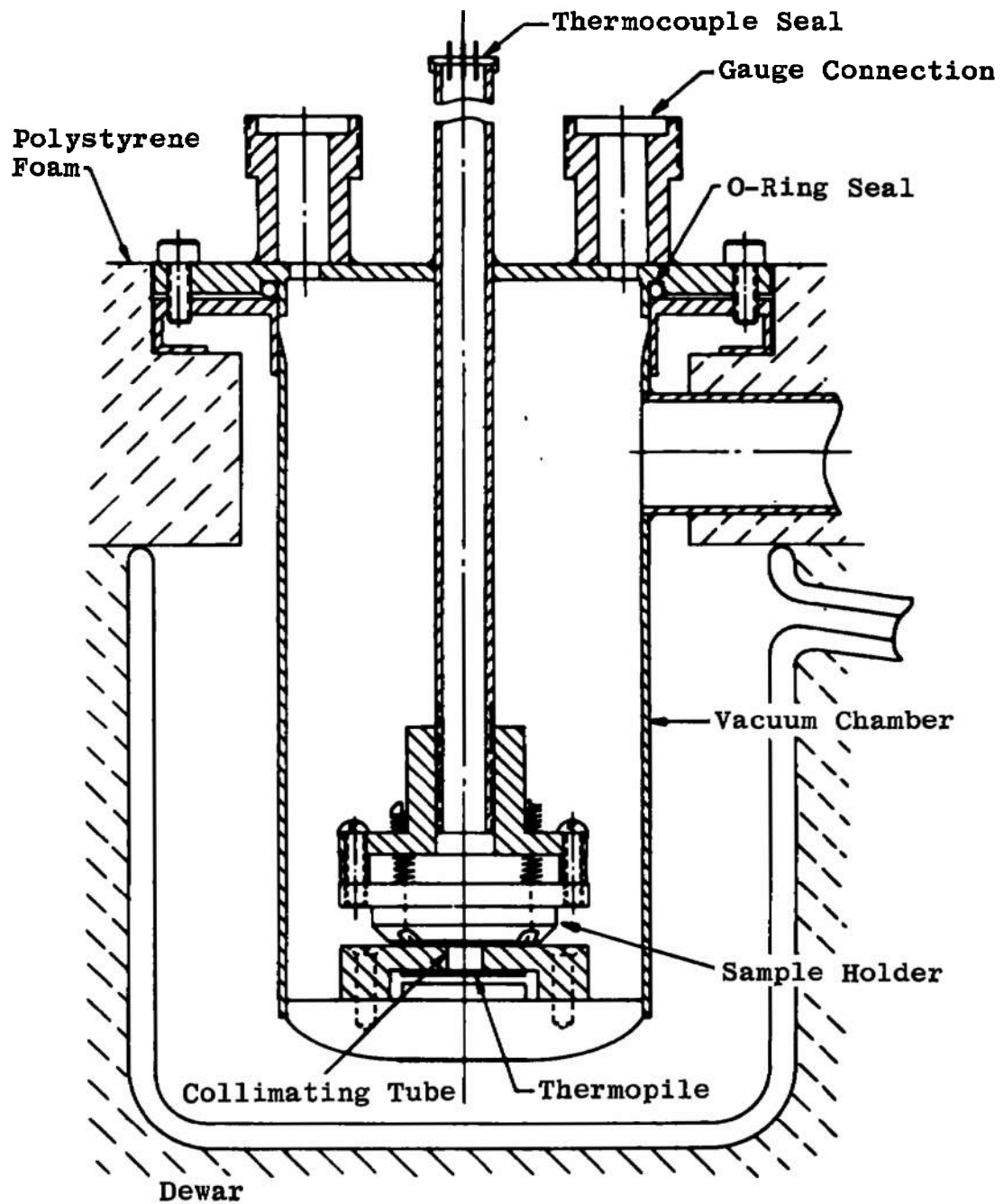


Figure 2. Total emissance calorimeter.

the spectral, bi-hemispherical reflectance,  $\rho_\lambda$ , of the surface. By Kirchhoff's law (1),  $\epsilon_\lambda = \alpha_\lambda$ , and for an opaque surface,  $(1 - \rho_\lambda) = \alpha_\lambda$ . Consequently,  $\epsilon_\lambda = (1 - \rho_\lambda)$  for opaque surfaces (see Chapter II). Therefore, by measuring  $\rho_\lambda$ ,  $\epsilon_\lambda$  is obtained, and the total hemispherical emittance,  $\epsilon$ , can be calculated for any desired surface temperature from Equation 5.

If the surface is gray, as is often a close approximation,  $\epsilon = \epsilon_\lambda$ , and the measurement of  $\rho_\lambda$  becomes a particularly convenient way to determine  $\epsilon$ .

However, prior to the present work, there has been no way to measure  $\rho_\lambda$  directly. The heated cavity reflectometer (Figure 3) of Dunkle, et al. (4), is widely used to determine the infrared, spectral, directional-hemispherical reflectance,  $\rho_{\lambda dh}(\theta, \phi)$ , which can be used in various ways to estimate  $\epsilon$ . For example, by another form of Kirchhoff's law, the spectral, directional emittance  $\epsilon_\lambda(\theta, \phi)$  is equal to  $[1 - \rho_{\lambda dh}(\theta, \phi)]$ , and  $\epsilon_\lambda$  can be calculated from heated cavity reflectometer data by integrating over a hemisphere (see Appendix A):

$$\epsilon_\lambda = \frac{1}{\pi} \int_0^{2\pi} \int_0^{\pi/2} \epsilon_\lambda(\theta, \phi) \cos\theta \sin\theta \, d\theta \, d\phi \quad (7)$$

With the result of this integration,  $\epsilon$  is calculated from Equation 5. There is one problem encountered in calculating  $\epsilon_\lambda$  from Equation 7, viz., the heated cavity cannot provide directional reflectance data in the  $75^\circ \leq \theta \leq 90^\circ$  region

8

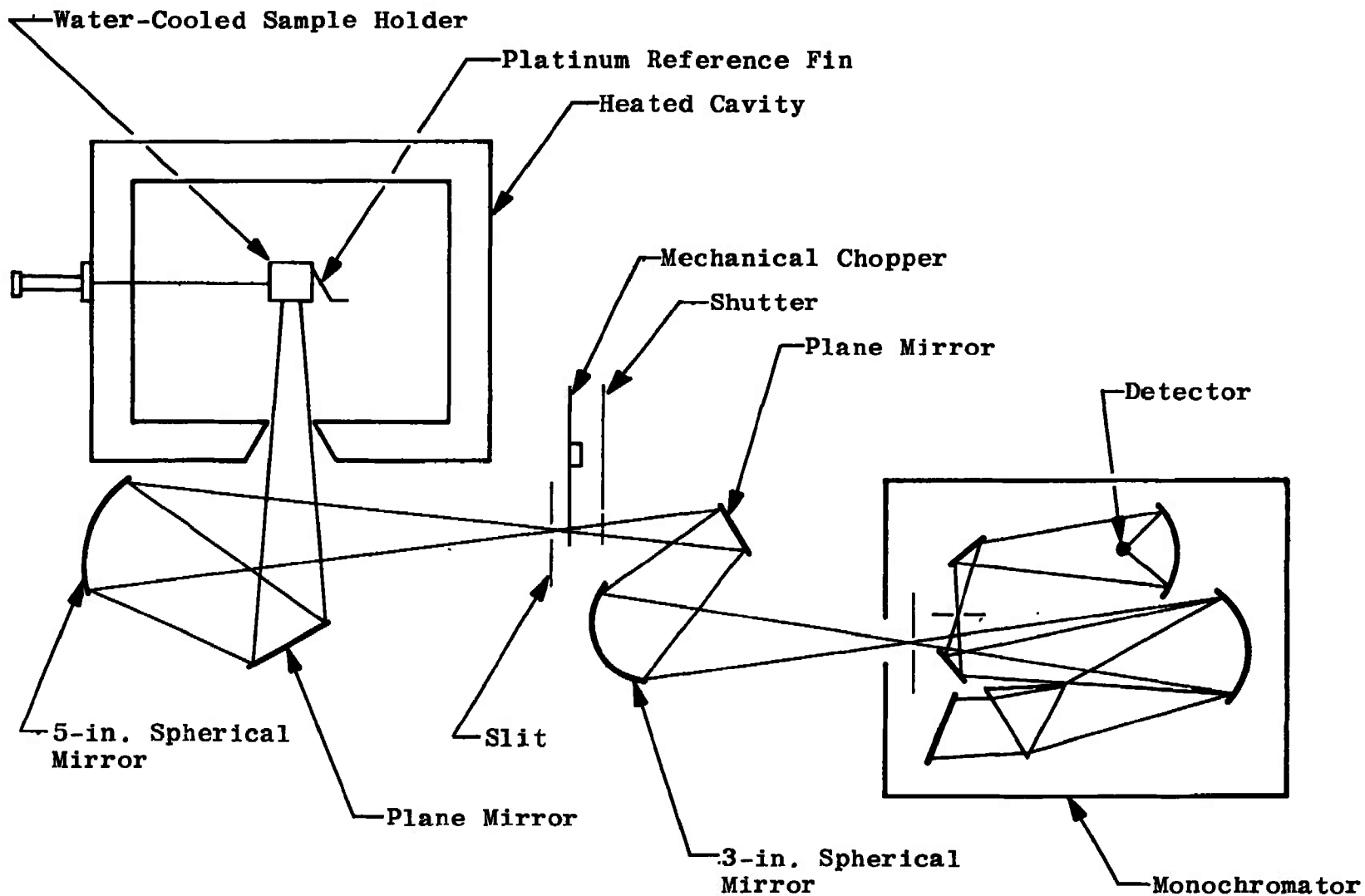


Figure 3. Schematic of directional reflectance apparatus.

because of the expanding monochromator slit image on the sample surface. This is a significant problem since metals exhibit decreasing reflectance (i.e., increasing emittance) in the 75 to 85 degree direction. To complete the calculation of  $\epsilon_\lambda$ , it is necessary to extrapolate  $\rho_{\lambda dh}(\theta, \phi)$  to 90 degrees and, consequently, introduce the possibility of an error.

Another way to apply the heated cavity reflectometer to determine  $\epsilon$  requires only a normal (actually a near-normal) measurement of reflectance from which the normal spectral emittance  $\epsilon_\lambda(0,0)$  is specified by Kirchhoff's law. The total normal emittance is then calculated from a form of Equation 5:

$$\epsilon_n = \frac{\int_{\lambda_1}^{\lambda_2} \epsilon_\lambda(0,0) e_{b\lambda}(T) d\lambda}{\int_{\lambda_1}^{\lambda_2} e_{b\lambda}(T) d\lambda} \quad (8)$$

Knowing  $\epsilon_n$ , it becomes possible to estimate  $\epsilon$  for the surface in question. This estimate follows from predictions which are based on electromagnetic theory and are summarized as follows (1):

1. For electric non-conductors,  $\epsilon_n$  is typically greater than 0.6 and  $0.95 \leq \epsilon/\epsilon_n \leq 1$ .
2. For metals,  $\epsilon_n$  is normally less than 0.1 and  $1.1 \leq \epsilon/\epsilon_n \leq 1.32$ .

In the final analysis, the heated cavity reflectance data provide only estimates of  $\epsilon$  and, as indicated previously, a technique for the measurement of spectral, bi-hemispherical, reflectance,  $\rho_\lambda$ , has not been available.

Magnesium oxide (MgO) coated, integrating spheres (5) and auxiliary spectrophotometry equipment have been widely used in commercial and non-commercial instruments for measuring spectral reflectance of surfaces in the 0.25 to 2.5 micron region. Depending on the design, integrating spheres may be used to measure either directional-hemispherical reflectance or hemispherical-directional reflectance. In this terminology, the first term specifies the manner in which the sample surface is irradiated and the second term specifies the manner in which the reflected power is measured. By reciprocity, directional-hemispherical reflectance at a specified direction of incident power is equal to hemispherical-directional reflectance of power in the specified direction.

These applications of integrating spheres strongly suggest that integrating spheres can also be used to measure hemispherical-hemispherical (i.e., bi-hemispherical) reflectance,  $\rho_\lambda$ . As indicated previously, this is a particularly worthwhile measurement since  $(1 - \rho_\lambda) = \epsilon_\lambda$  for opaque surfaces. The present work is directed toward the development of a technique for the direct measurement of  $\rho_\lambda$  using an infrared integrating sphere.

## CHAPTER II

## ANALYSIS

I. ANALYSIS OF A TECHNIQUE FOR MEASURING  
BI-HEMISPHERICAL REFLECTANCE WITH  
AN INTEGRATING SPHERE

One very useful form of Kirchhoff's law specifies that the monochromatic, directional emittance,  $\epsilon_\lambda(\theta, \phi)$ , of a surface is equal to the monochromatic, directional absorptivity  $\alpha_\lambda(\theta, \phi)$  of the surface when the surface temperature is held constant (6). The quantity  $\alpha_\lambda(\theta, \phi)$  is defined as the fraction of incident power, flowing from the  $(\theta, \phi)$  direction, which is absorbed by the surface. For an opaque surface, the conservation of energy requires that

$$\alpha_\lambda(\theta, \phi) = [1 - \rho_{\lambda dh}(\theta, \phi)] \quad (9)$$

where  $\rho_{\lambda dh}(\theta, \phi)$  is the monochromatic, directional-hemispherical reflectance of the surface when irradiated from the  $(\theta, \phi)$  direction. Therefore, by Kirchhoff's law:

$$\epsilon_\lambda(\theta, \phi) = [1 - \rho_{\lambda dh}(\theta, \phi)] \quad (10)$$

Further, the hemispherical and the directional emittances are related as follows (see Appendix A):

$$\epsilon_\lambda = \frac{1}{\pi} \int_0^{2\pi} \int_0^{\pi/2} \epsilon_\lambda(\theta, \phi) \cos\theta \sin\theta \, d\theta \, d\phi \quad (11)$$

By substituting Equation 10 into Equation 11, the following relation between hemispherical emittance and directional-hemispherical reflectance is obtained:

$$\epsilon_{\lambda} = 1 - \frac{1}{\pi} \int_0^{2\pi} \int_0^{\pi/2} \rho_{\lambda dh}(\theta, \phi) \cos\theta \sin\theta \, d\theta \, d\phi \quad (12)$$

The integral term is the monochromatic, hemispherical-hemispherical (i.e., bi-hemispherical) reflectance  $\rho_{\lambda}$ , Reference (7):

$$\rho_{\lambda} = \frac{1}{\pi} \int_0^{2\pi} \int_0^{\pi/2} \rho_{\lambda dh}(\theta, \phi) \cos\theta \sin\theta \, d\theta \, d\phi \quad (13)$$

Physically,  $\rho_{\lambda}$  is the fraction of incident power which is reflected from a surface when the surface is uniformly, hemispherically irradiated.

The object of the present analysis is to demonstrate that an integrating sphere can be applied to accomplish the double integration required in Equation 13. To this end, consider an arrangement in which a small sample, of area  $A_s$ , is wall-mounted on a port looking into an integrating sphere (Figure 4) whose interior is coated with a diffusing, highly reflecting material of reflectance  $\rho_w$ . Let monochromatic power,  $P_o$ , pass into the sphere through a second port, suffer its first reflection at the sphere wall, disperse to the sphere interior and suffer a second reflection at the sphere wall. Baffles are provided so that no first reflection power strikes either the sample surface or the infrared



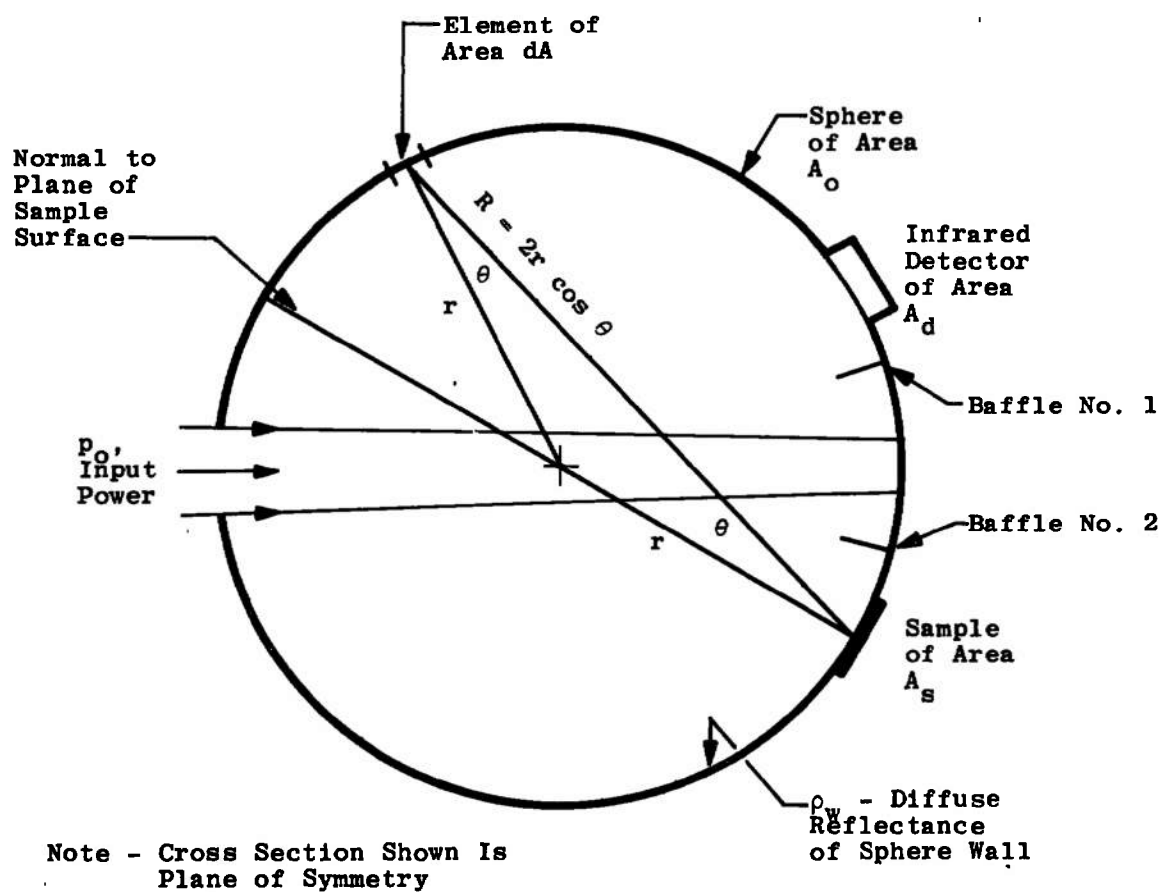


Figure 4. Integrating sphere and associated components for bi-hemispherical reflectance measurements.

detector. After the second wall reflection, a portion of the power will hemispherically irradiate and reflect from the sample. The reflected component will again reflect off the sphere wall and a portion of this component will strike the detector and contribute to its output. Baffle Number 2, Figure 4, is sized to prevent any reflected energy from going directly from sample to detector.

The objective at this point in the analysis is to calculate an expression for that fraction of the first component of power which is reflected from the sample and which gets to the detector (see Equation 23). After  $P_o$  strikes the wall between the baffles (Figure 4), the portion of the first wall reflection which goes to differential sphere area,  $dA$ , is

$$P_{1 \rightarrow dA} = \rho_w P_o \left( \frac{dA}{A_o} \right) \quad (14)$$

where  $(dA/A_o)$  is the shape factor for transfer of energy from the illuminated area on the wall to  $dA$  (see Appendix B). The portion of the second reflection power going to the sample from  $dA$  is

$$dP_{2 \rightarrow s} = \rho_w^2 P_o \left( \frac{dA}{A_o} \right) \left( \frac{A_s}{A_o} \right) \quad (15)$$

where  $(A_s/A_o)$  is the shape factor between  $dA$  and the sample. Now define  $d\omega$  as the solid angle determined by  $dA$  and  $R$  (Figure 4):

$$d\omega = \frac{dA \cos \theta}{R^2} = \frac{dA \cos \theta}{4r^2 \cos^2 \theta} \quad (16)$$

$$d\omega = \frac{dA}{4r^2 \cos\theta} \quad (17)$$

Then the second reflection power per unit solid angle transferred from  $dA$  to  $A_s$  is the ratio of Equations 15 and 17:

$$\frac{dP_{2 \rightarrow s}}{d\omega} = \frac{\rho_w^2 P_o \left( \frac{dA}{A_o} \right) \left( \frac{A_s}{A_o} \right)}{\frac{dA}{4r^2 \cos\theta}} \quad (18)$$

Since  $A_o = 4\pi r^2$ ,

$$\frac{dP_{2 \rightarrow s}}{d\omega} = \frac{\rho_w^2 P_o}{\pi} \cos\theta \left( \frac{A_s}{A_o} \right) \quad (19)$$

The azimuthal angle,  $\phi$ , has not entered the argument so far because  $[dP_{2 \rightarrow s}/d\omega]$  will be independent of  $\phi$  in an ideal integrating sphere.

To find the total amount of second wall reflection energy which is reflected off the sample, multiply Equation 19 by  $\rho_{dh}(\theta, \phi)$  of the sample and integrate over the hemispherical space "above" the sample:

$$P_{2 \rightarrow s \rightarrow w} = \int_0^{\pi/2} \frac{\rho_w^2 P_o}{\pi} \rho_{dh}(\theta, \phi) \cos\theta \left( \frac{A_s}{A_o} \right) d\omega \quad (20)$$

This power suffers another wall reflection and a fraction  $(A_d/A_o)$  of the reflected power finally reaches the detector:

$$P_{2 \rightarrow s \rightarrow w \rightarrow \text{detector}} = \int_0^{\pi/2} \frac{\rho_w^3 P_o}{\pi} \rho_{dh}(\theta, \phi) \cos\theta \left( \frac{A_s}{A_o} \right) \left( \frac{A_d}{A_o} \right) d\omega \quad (21)$$

Since  $d\omega = \sin\theta \, d\theta \, d\phi$ , the integral becomes

$$P_{2 \rightarrow s \rightarrow w \rightarrow \text{detector}} = \frac{\rho_w^3 P_o A_s A_d}{A_o^2} \cdot \frac{1}{\pi} \int_0^{2\pi} \int_0^{\pi/2} \rho_{dh}(\theta, \phi) \cos\theta \sin\theta \, d\theta \, d\phi \quad (22)$$

According to Equation 13, the integral in Equation 22 represents the bi-hemispherical reflectance of the surface for the wavelength of  $P_o$ . Therefore, this detected component is proportional to  $\rho_\lambda$ :

$$P_{2 \rightarrow s \rightarrow w \rightarrow \text{detector}} = K_1 \rho_\lambda \quad (23)$$

Additional wall-reflected components suffer three, four, five, etc., reflections at the wall before irradiating the sample. A similar argument applies to each of these components:

$$\begin{array}{lcl} P_{3 \rightarrow s \rightarrow w \rightarrow \text{detector}} & = & K_2 \rho_\lambda \\ P_{4 \rightarrow s \rightarrow w \rightarrow \text{detector}} & = & K_3 \rho_\lambda \end{array} \quad (24)$$

Summing all components indicates that a portion of the power reaching the detector is linearly related to the bi-hemispherical reflectance of the sample. This relationship (Equation 30) is examined in much more detail in the following section. At present, however, it is obvious that most of

the power reaching the detector will be wall-reflected components which never strike the sample (see Equation 32). Therefore, the detector output voltage will be of the form

$$E_o = E + \Delta E \quad (25)$$

where  $\Delta E = K\rho_\lambda$ . It follows, therefore, that if  $\Delta E$  is large enough relative to  $E$  to be measured accurately, then the integrating sphere can be applied to the determination of  $\rho_\lambda$  (i.e.,  $\epsilon_\lambda$ ). The calibration constant,  $K$ , could be determined by measuring  $\Delta E$  for a surface of known infrared  $\rho_\lambda$ .

## II. CALCULATION OF $(\Delta E/E)$

The input power,  $P_o$ , separates into an infinite number of components by inter-reflections within the sphere. Figure 5 indicates the manner in which the input energy disperses. The object at this time is to derive an expression for the power included in all components reaching the detector,  $A_d$ . Sub-components which have been reflected off the sample three or more times will be excluded from the analysis. This is justified on the basis that the shape factor ( $A_s/A_o$ ) will be of order  $10^{-2}$ , and the power contained in components reflected from the sample will be attenuated by orders of  $10^{-2N}$  where  $N$  is the number of sample reflections which have occurred.

Figure 6 shows the power of each reflected component of Branch Number 1 (Figure 5). These values follow from the straightforward application of the shape factor for energy

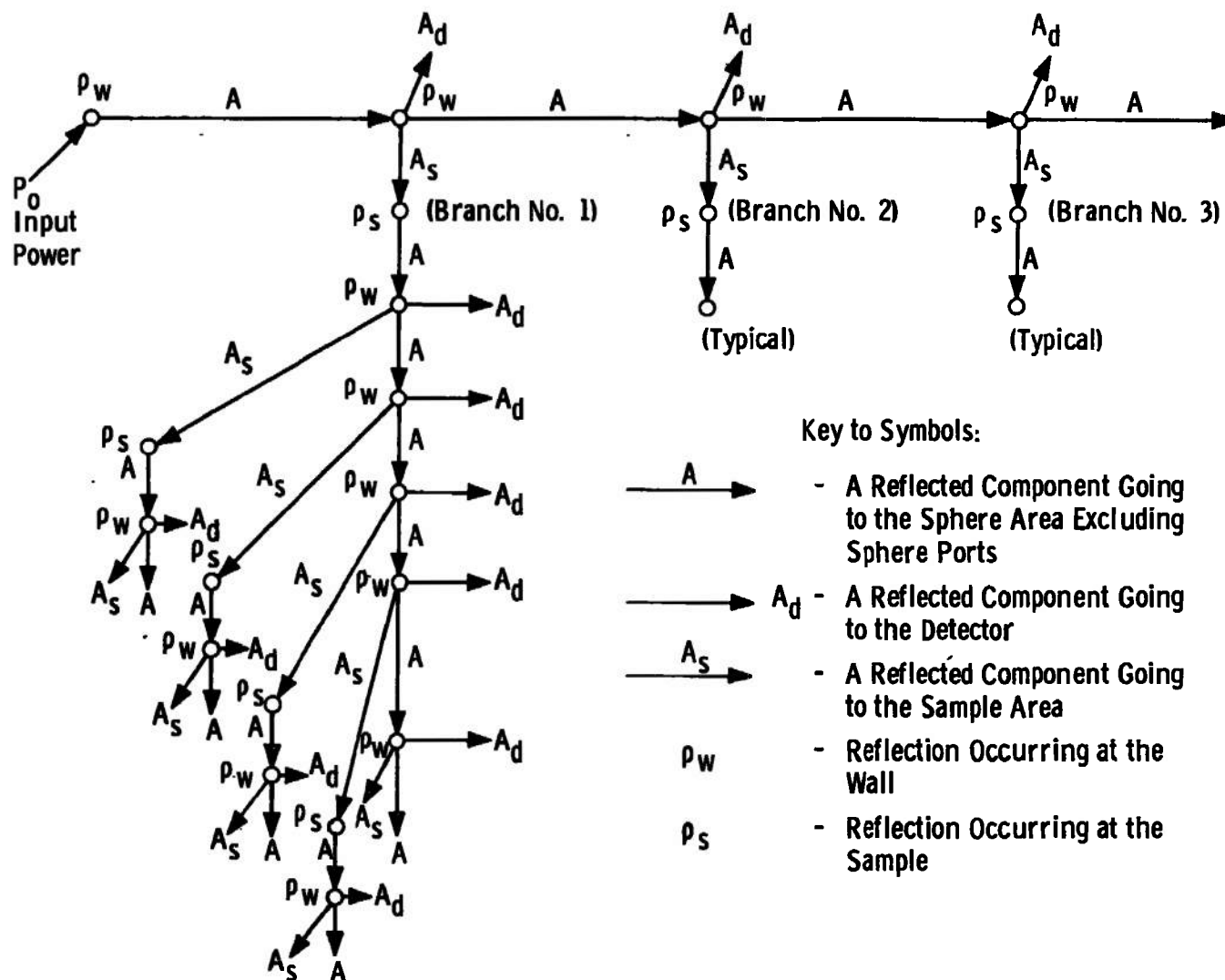


Figure 5. Inter-reflection components.

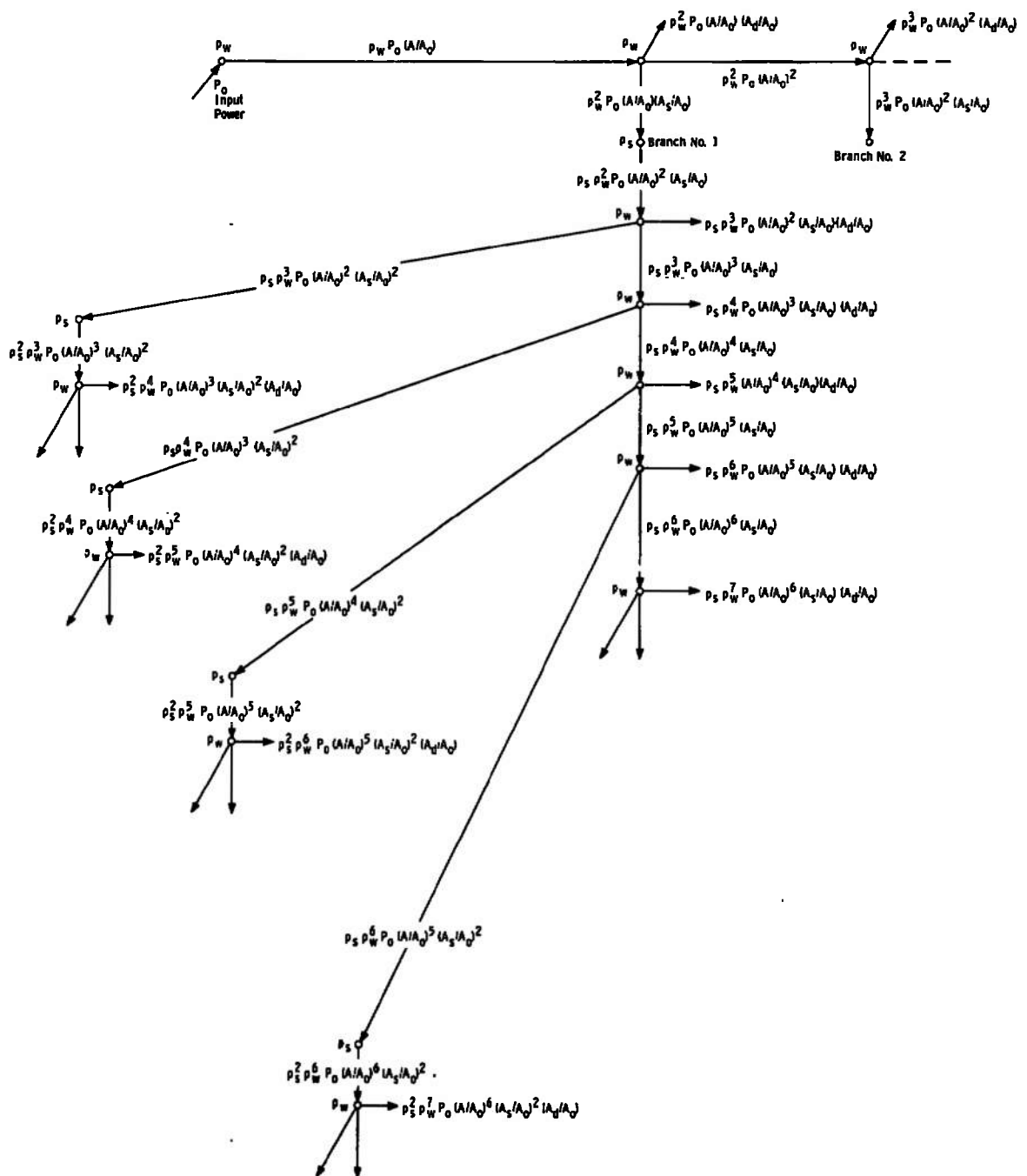


Figure 6. Power retained in inter-reflection components.

transfer between one area and another on the surface of an ideal integrating sphere (see Appendix B). Summing all detector components in Branch Number 1 gives

$$\begin{aligned} \Delta P_1 = & \rho_s \rho_w^3 P_o \left( \frac{A}{A_o} \right)^2 \left( \frac{A_s}{A_o} \right) \left( \frac{A_d}{A_o} \right) \left[ 1 + \frac{\rho_w A}{A_o} + \frac{\rho_w^2 A^2}{A_o^2} \right. \\ & \left. + \frac{\rho_w^3 A^3}{A_o^3} + \dots \right] + \rho_s^2 \rho_w^4 P_o \left( \frac{A}{A_o} \right)^3 \left( \frac{A_s}{A_o} \right)^2 \left( \frac{A_d}{A_o} \right) \\ & \cdot \left[ 1 + \frac{\rho_w A}{A_o} + \frac{\rho_w^2 A^2}{A_o^2} + \frac{\rho_w^3 A^3}{A_o^3} + \dots \right] \end{aligned} \quad (26)$$

Since  $(\rho_w A/A_o)$  is less than unity, the series in parentheses will converge to  $[1 - (\rho_w A/A_o)]^{-1}$ , and

$$\begin{aligned} \Delta P_1 = & \left[ \rho_s \rho_w^3 P_o \left( \frac{A}{A_o} \right)^2 \left( \frac{A_s}{A_o} \right) \left( \frac{A_d}{A_o} \right) \right] \left[ 1 + \rho_s \rho_w \left( \frac{A}{A_o} \right) \left( \frac{A_s}{A_o} \right) \right] \\ & \cdot \left[ \frac{1}{1 - (\rho_w A/A_o)} \right] \end{aligned} \quad (27)$$

It is convenient at this point to stipulate that  $(A_s/A_o)$  shall be of order  $10^{-2}$ . Since  $\rho_s$ ,  $\rho_w$  and  $A/A_o$  are all less than unity, the middle term in Equation 27 becomes unity to within 1 per cent. Therefore

$$\Delta P_1 \approx \frac{\rho_s \rho_w^3 P_o \left( \frac{A}{A_o} \right)^2 \left( \frac{A_s}{A_o} \right) \left( \frac{A_d}{A_o} \right)}{[1 - \rho_w (A/A_o)]} \quad (28)$$



Power components similar to Equation 28 will also come from the other branches (Figures 5 and 6, pages 18 and 19). However, each component will be a factor of  $(\rho_w A/A_o)$  less than the preceding component. Consequently, the total component of detector power which varies with  $\rho_s$  can be written:

$$\Delta P \approx \frac{\rho_s \rho_w^3 P_o \left(\frac{A}{A_o}\right)^2 \left(\frac{A_s}{A_o}\right) \left(\frac{A_d}{A_o}\right)}{[1 - \rho_w (A/A_o)]} \left( 1 + \rho_w \left(\frac{A}{A_o}\right) + \rho_w^2 \left(\frac{A}{A_o}\right)^2 + \dots \right) \quad (29)$$

Therefore:

$$\Delta P \approx \frac{\rho_s \rho_w^3 P_o \left(\frac{A}{A_o}\right)^2 \left(\frac{A_s}{A_o}\right) \left(\frac{A_d}{A_o}\right)}{[1 - \rho_w (A/A_o)]^2} \quad (30)$$

The detector components at the top of Figures 5 and 6 are wall reflected components which are not a function of  $\rho_s$ . The sum of these components is

$$P = \rho_w^2 P_o \left(\frac{A}{A_o}\right) \left(\frac{A_d}{A_o}\right) \left( 1 + \rho_w \left(\frac{A}{A_o}\right) + \rho_w^2 \left(\frac{A}{A_o}\right)^2 + \dots \right) \quad (31)$$

Therefore:

$$P = \frac{\rho_w^2 P_o \left(\frac{A}{A_o}\right) \left(\frac{A_d}{A_o}\right)}{[1 - \rho_w (A/A_o)]} \quad (32)$$

Since the detector output voltage is the product of power

reaching the detector and the detector sensitivity,  $\Delta E/E$  is the ratio of Equations 30 and 32:

$$\frac{\Delta E}{E} \approx \frac{\rho_s \rho_w \left( \frac{A}{A_o} \right) \left( \frac{A_s}{A_o} \right)}{[1 - \rho_w (A/A_o)]} \quad (33)$$

The magnitude of  $\Delta E/E$  can be evaluated by noting that typical values for  $\rho_w$  and  $A/A_o$  are 0.95 and 0.98, respectively, while  $A_s/A_o$  has been set at  $10^{-2}$ . With these values

$$\frac{\Delta E}{E} \approx 13.3 \cdot 10^{-2} \rho_s \quad (34)$$

This result suggests that with stable instruments, and conditions,  $\rho_s$  can be accurately determined by measuring  $\Delta E$ . For example, a reflectance change of 0.01 (i.e., 1 per cent on a scale of 100 per cent) will generate a  $\Delta E$  of

$$\Delta E \approx 1.34 \cdot 10^{-3} E \quad (35)$$

This indicates that the voltage measurement will have to be resolved to within approximately  $\pm 1$  part per thousand in order to determine  $\rho_s$  within  $\pm 1$  per cent on a full range scale of 100 per cent reflectance. This resolution is feasible with modern instrumentation provided  $E$  is stable and sufficiently large.

## CHAPTER III

## INFRARED REFLECTOMETER DESIGN

I. DESCRIPTION OF AN INFRARED BI-  
HEMISPHERICAL REFLECTOMETER

The spectroreflectometer shown schematically in Figure 7, and pictorially in Figures 8 and 9, was designed and developed to implement the bi-hemispherical reflectance measurement technique which was analyzed in Chapter II. In operation, energy from the infrared source is collected by the gold-coated, 6-inch mirror (Figure 7) and is focussed at the entrance slit of the monochromator. The energy is dispersed by a cesium bromide (CsBr) prism in the Perkin-Elmer Model 98 monochromator, and a selectable, narrow band of infrared frequencies exits the monochromator. The CsBr prism is usable over the infrared region from 1 to 38 microns ( $\mu$ ). After leaving the monochromator, the energy is chopped at 100 Hz and is collected by the gold-coated, 8-inch mirror and focussed into the infrared integrating sphere. Details of the sphere are shown in Figure 9. A small portion of the input power is measured by the input power detector which is mounted on the integrating sphere behind the narrow, centrally located slit between the baffles. This detector signal is used by the slit servo instrumentation to maintain the input power constant during a measurement.

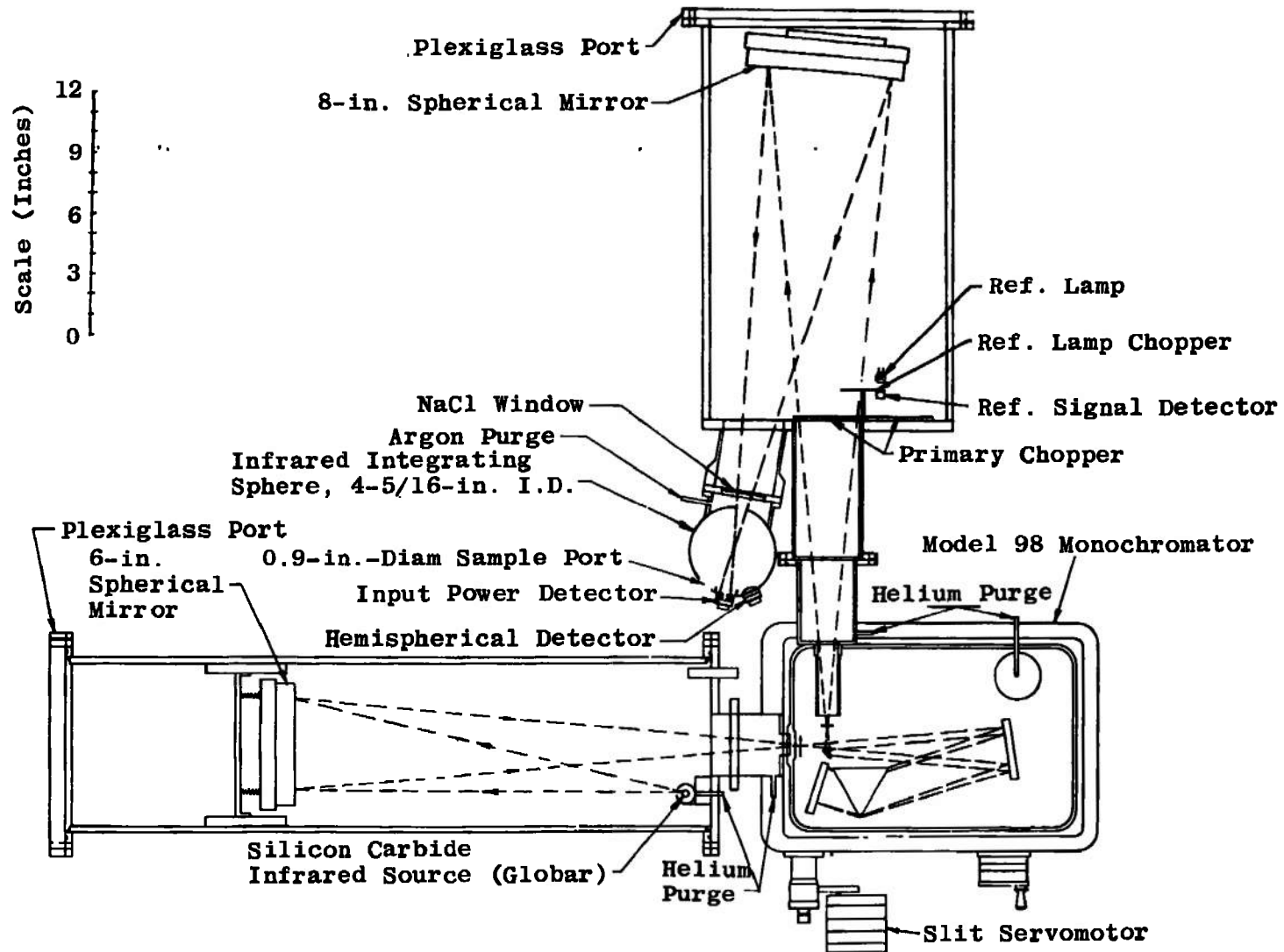


Figure 7. Infrared bi-hemispherical reflectometer schematic.

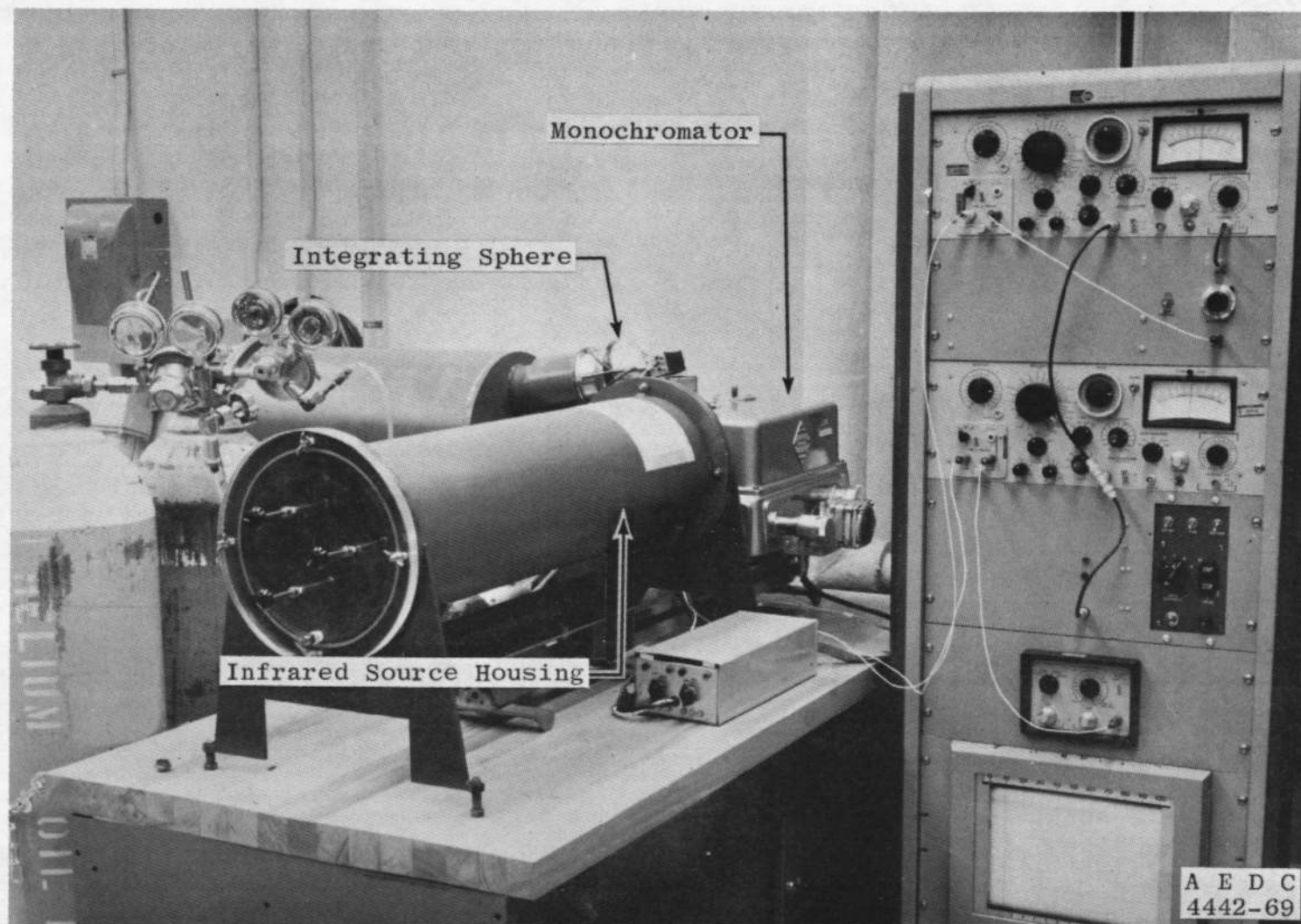


Figure 8. Infrared bi-hemispherical reflectometer photograph.

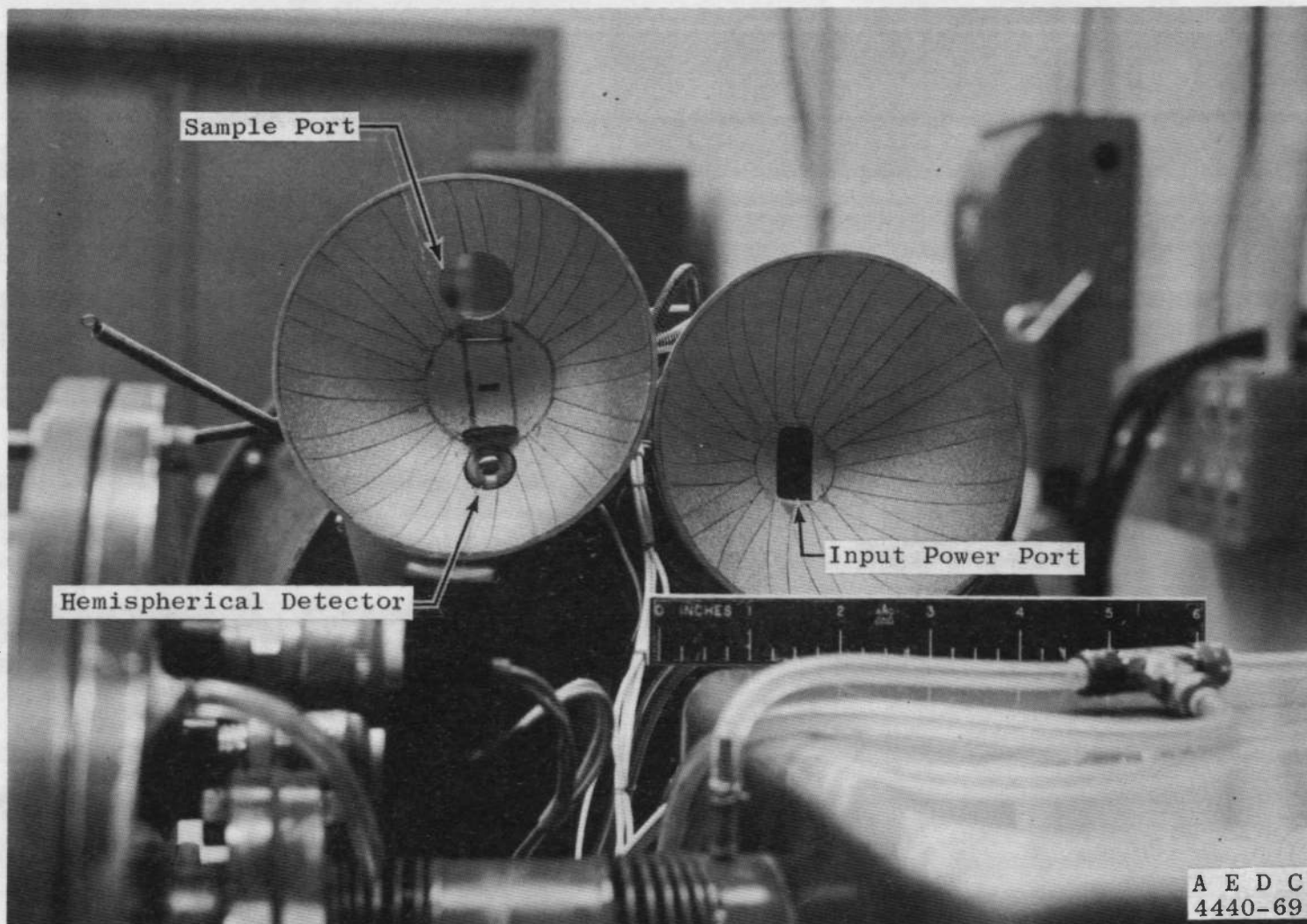


Figure 9. Details of interior of infrared integrating sphere.

The remainder of the input power is scattered over the sphere interior by an initial wall reflection from the area between the baffles. The baffles prevent any of this first reflection energy from getting to the sample port or to the hemispherical detector. They also prevent any of the energy which is reflected from the sample from going directly to the hemispherical detector. The inter-reflections which occur within the sphere were fully examined in Chapter II. The sample on the 0.9-inch diameter sample port is hemispherically illuminated; and since the ratio of sample area to sphere area is  $(A_s/A_o) = 0.0109$  (i.e., approximately  $10^{-2}$ ), the output of the hemispherical detector can be expected to be of the form  $E + \Delta E$  where  $\Delta E$  is proportional to the bi-hemispherical reflectance of the sample surface as specified in Equation 33.

In order to maximize the transmission of infrared energy through the system, no monochromator windows were used. Also, to prevent atmospheric absorption of the energy, the 6- and 8-inch mirror enclosures were made airtight and are helium purged as a unit which includes the monochromator housing. The infrared integrating sphere is also purged to prevent atmospheric absorption. This is particularly important since atmospheric absorption within the sphere would have the same disastrous effect on the magnitude of the hemispherical detector signal as would a low wall reflectance.

The infrared detection and slit control

instrumentation for the reflectometer is shown schematically in Figure 10. The two detectors are Barnes Engineering, thermistor infrared detectors. Each detector has both an active thermistor flake, which is blackened and is exposed to the infrared radiation, and an adjacent compensation flake which is shielded from the radiation. The thermistor flakes are 2.5 mm by 2.5 mm by 10 microns thick and have a negative temperature coefficient of 4 per cent per °C.

They are operated in a full bridge as shown in Figure 10 and are biased to  $\pm 510$  V with batteries. The signal reference point is the common lead between the pair of batteries.

When radiation strikes the active flake its temperature rises and its resistance decreases. Since the resistance of the compensation flake remains unchanged, a resistive imbalance is generated and causes a change in the potential at the common lead between the flakes. This voltage change is proportional to the magnitude of the incident irradiance.

Thermistor detectors were chosen for use in the reflectometer because broadband (i.e., 1 - 35  $\mu$ ) types were readily available commercially. Also, thermistor detector responsivities for 6.25 mm<sup>2</sup> active thermistor flakes range from 50 to 100 volts/watt as compared to the 5 to 15 volts/watt generated by thermopile infrared detectors of comparable receiver area.

The two detector signals are read out on two separate Princeton Applied Research Model HR-8 lock-in amplifiers. These amplifiers synchronously rectify the detector signals



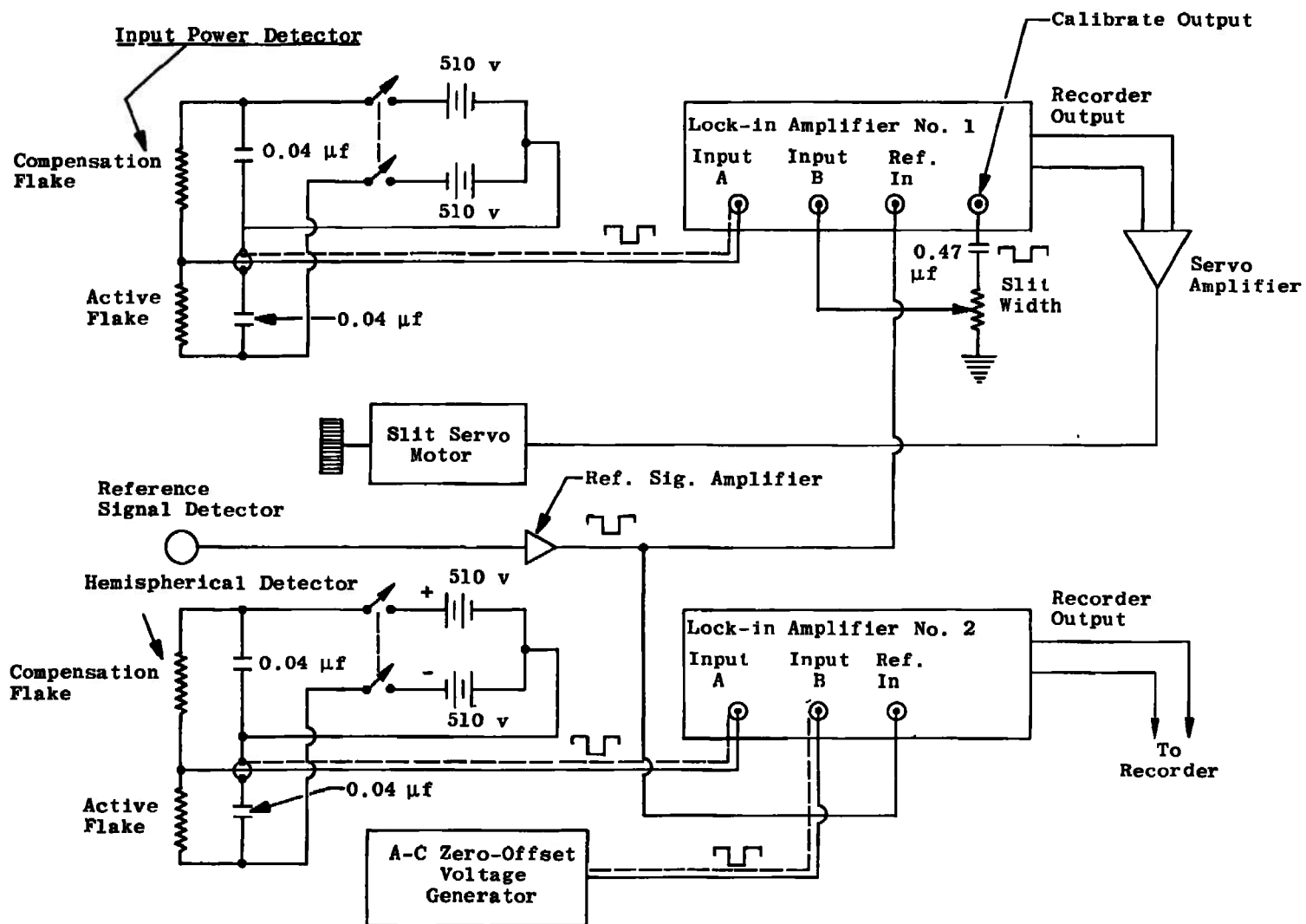


Figure 10. Block diagram of the infrared detection and slit control instrumentation.

and function as narrow band detection systems. The amplifiers utilize the reference signal which is generated by the auxiliary chopper blade and the reference lamp and detector indicated in Figure 7, page 24. In simplest terms, each amplifier receives a square-wave detector signal and a square-wave reference signal. Only the fundamental component of the detector signal is amplified and all harmonics are filtered out. This component may be designated  $e_s(t) = GE_s(t)\sin\omega t$  where  $E_s(t)$  is the peak amplitude of the fundamental component of the hemispherical detector signal and  $G$  is the amplification gain factor. Similarly, the fundamental component of the reference signal is amplified to unity peak amplitude and may be designated  $e_r(t) = \sin\omega t$ . These two signals are multiplied in a mixer stage to obtain an output of

$$e_m(t) = GE_s(t) \sin^2\omega t \quad (36)$$

Since  $\sin^2\omega t = [1/2(1 - \cos 2\omega t)]$ ,

$$e_m(t) = [1/2 GE_s(t)] - [1/2 GE_s(t)\cos 2\omega t] \quad (37)$$

Therefore, the mixer output contains the slowly varying D.C. component,  $[1/2 GE_s(t)]$ , and an A.C. signal which is eliminated by filtering the output. The D.C. component is amplified and presented as the output signal. The HR-8 amplifiers are calibrated in terms of the rms value of the fundamental component of the detector signal. The sensitivity is adjustable from 100 nanovolts (nv) to 500

millivolts (mv) full scale in 21 ranges.

A narrow amplifier bandwidth is obtained by filtering the D.C. output component. The bandwidth is given by  $\Delta B = (1/8RC)$ , where  $RC$  is the output time constant and is adjustable from 1 msec to 100 seconds. The amplifier rise time (10 to 90 per cent) is given by  $T_r = 3.4 RC$ .

Both of the HR-8 amplifiers (Figure 10, page 29) have differential input pre-amplifiers which are utilized to take the difference between two input signals. The signal from the input power detector is compared to a standard calibration signal and the difference signal is amplified and used to servo the monochromator slits for maintaining a constant, sphere-input power.

The signal from the hemispherical detector is compared to the offset generator output (Figure 10) and is nulled when there is no sample on the sphere sample port. Nulling is accomplished by varying the amplitude and phasing of the output of the offset generator. After nulling is accomplished the sensitivity of amplifier number 2 can be increased to display and record the  $\Delta E$  resulting from placing a sample on the sample port.

Data is collected as follows. The monochromator is adjusted to the wavelength band of interest and the hemispherical detector reading is nulled with the sample port open. The sensitivity of amplifier number 2 is increased by a factor of 10 and final nulling is then accomplished by adjusting the offset generator for a zero recorder

deflection. A standard gold mirror is placed on the sample port and the resulting  $(\Delta E)_g$  is recorded. The standard is then replaced with the sample and the resulting  $(\Delta E)$  is recorded. The spectral, bi-hemispherical reflectance  $(\rho_\lambda)_s$  of the sample is then calculated:

$$(\rho_\lambda)_s = \frac{(\rho_\lambda)_g}{(\Delta E)_g} (\Delta E) \quad (38)$$

Therefore, the measurement is relative to the spectral, bi-hemispherical reflectance,  $(\rho_\lambda)_g$ , of the standard gold mirror. An example of the recorded data for a standard gold mirror and two sample surfaces is shown in Figure 11.

## II. SIGNIFICANT DESIGN PROBLEMS

The performance of an infrared integrating sphere depends most strongly upon the reflectance of the sphere coating. This is clearly indicated in Equations 32 and 33. The sphere coating should have near-unity reflectance for all infrared wavelengths and should reflect diffusely. During this study, several types of surfaces were fabricated and tested. The most satisfactory were gold coated, silicon carbide (SiC) abrasive papers and gold coated monolayers of 60 to 80 mesh glass beads which were cemented to a substrate with a very thin layer of epoxy. Samples of five different grades of SiC abrasive papers were gold coated and tested. The test consisted of measuring the infrared reflectance in a Gier-Dunkle, heated cavity reflectometer similar to that

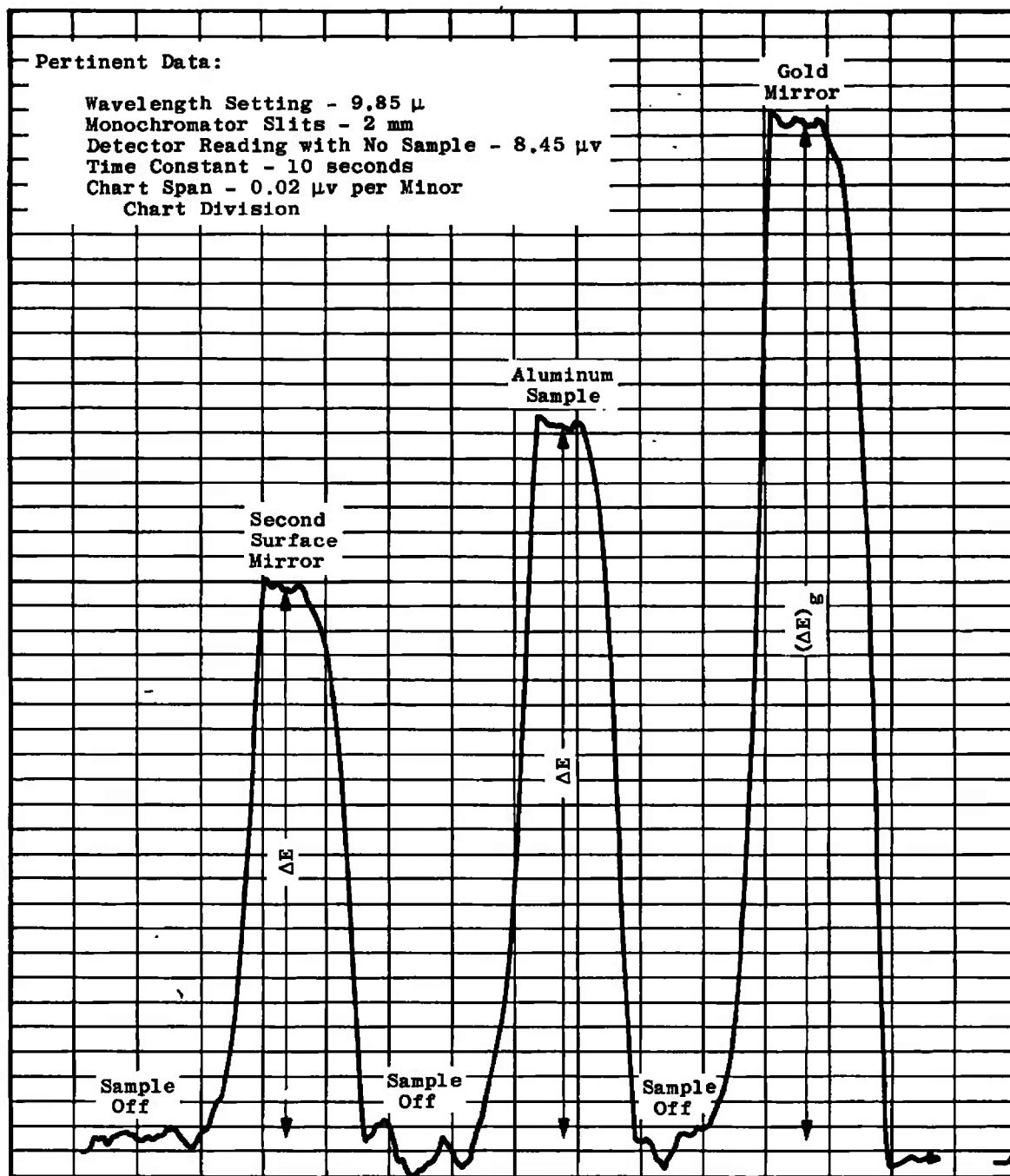


Figure 11. Example of reflectometer data for a gold mirror, a sand blasted aluminum surface and a second surface quartz mirror.

shown in Figure 3, page 8. The diffuse, hemispherical-directional reflectance at  $\theta = 0^\circ$  was measured after removing the platinum reference fin and rotating the sample holder until the normal to the sample was directed out the cavity exit port. This eliminated the specular component from the measured energy. The diffuse reflectance was then obtained by ratioing the energy reflected from the sample to the energy emitted from the top of the heated cavity. Figure 12 shows the resulting diffuse reflectance values at  $10\mu$  plotted against grit size and indicates that 180 grit has the highest reflectance (95.3 per cent).

In addition to these measurements, the total (i.e., diffuse plus specular) hemispherical-directional reflectances of the 180 grit surface and the glass beaded surface were determined for the range  $15^\circ \leq \theta \leq 70^\circ$  with the Gier-Dunkle reflectometer. The resulting reflectance values were found to be essentially independent of both direction and wavelength ( $1\mu - 15\mu$ ). The diffuse plus specular reflectance of the 180 grit surface was noted to be the same at  $\theta = 15^\circ$  as the diffuse reflectance at  $\theta = 0^\circ$ . This shows that the specular reflectance of the 180 grit surface is negligibly small. This fact, together with the fact that  $\rho(\theta)$  is constant with  $\theta$ , shows that the 180 grit surface functions as a diffuse reflector.

The directional reflectance values for the 180 grit surface and the glass beaded surface were multiplied by  $\cos \theta$  and plotted in the conventional manner in Figure 13.

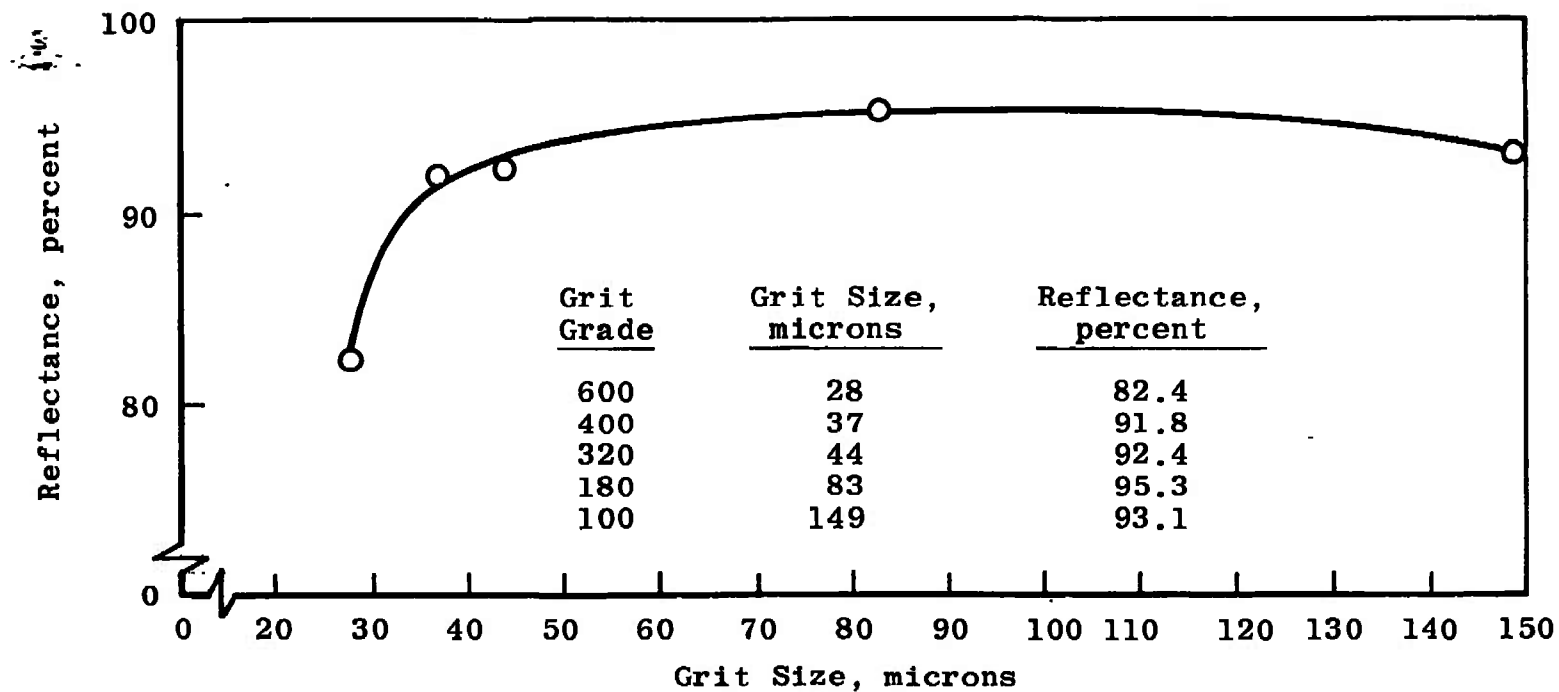


Figure 12. Diffuse component of hemispherical-directional reflectance in the normal direction ( $\theta = 0^\circ$ ) at  $10\mu$  for gold coated silicon carbide abrasive papers of varying grit sizes.

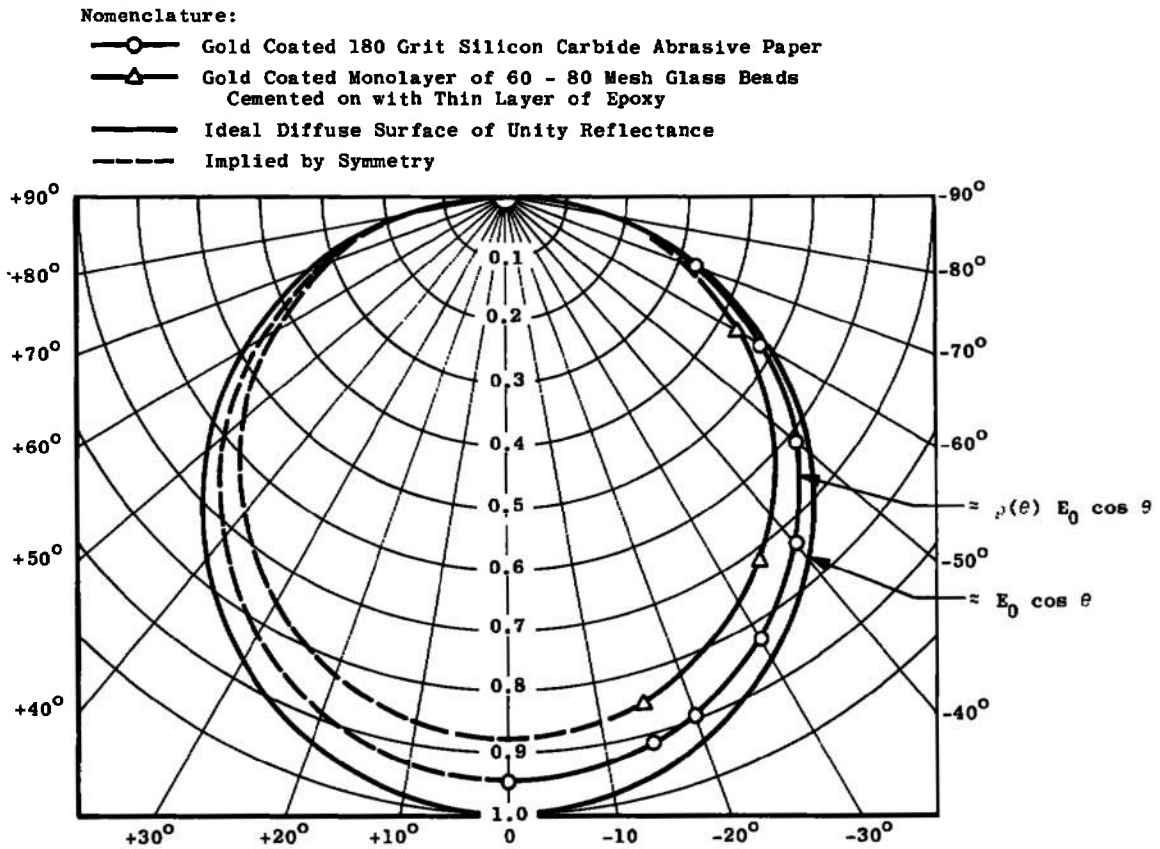


Figure 13. Theoretical, normalized distributions of  $10\mu$  energy reflected from directionally illuminated samples.



This type of plot characterizes the reflected flux distribution as a function of  $\theta$ . Since the 180 grit surface had a higher reflectance than the beaded surface, it was used in the fabrication of the integrating sphere (see Figure 9, page 26).

Another problem relating to the design of the reflectometer concerns the directional sensitivity of the hemispherical detector. The application of the  $(A_d/A_o)$  shape factor in calculating the power reaching the detector (Equation 32) assumes that the detector is Lambertian. The criterion for a Lambertian detector is that the detector signal vary as  $\cos \theta$ , where  $\theta$  is the angle between the detector normal and the incident flux.

The original detector acquired for use as the hemispherical detector was equipped with a flat KRS-5 window. The directional sensitivity of this detector was determined at approximately  $3\mu$  in normal planes and is shown in Figures 14a and 14b. The data were normalized to the detector readings in the normal direction and are plotted along with  $\cos \theta$  for comparison.

These plots show that the sensitivity is too high in the range  $20^\circ \leq \theta \leq 54^\circ$ . This was attributed to the reflection characteristics of the KRS-5 window, since there was no reason to suspect that the active thermistor flake would not function as a Lambertian detector. Consequently, a specially ground and polished KRS-5 hemispherical dome (0.400" I.D. x 0.600" O.D.) was purchased and sent to Barnes Engineering

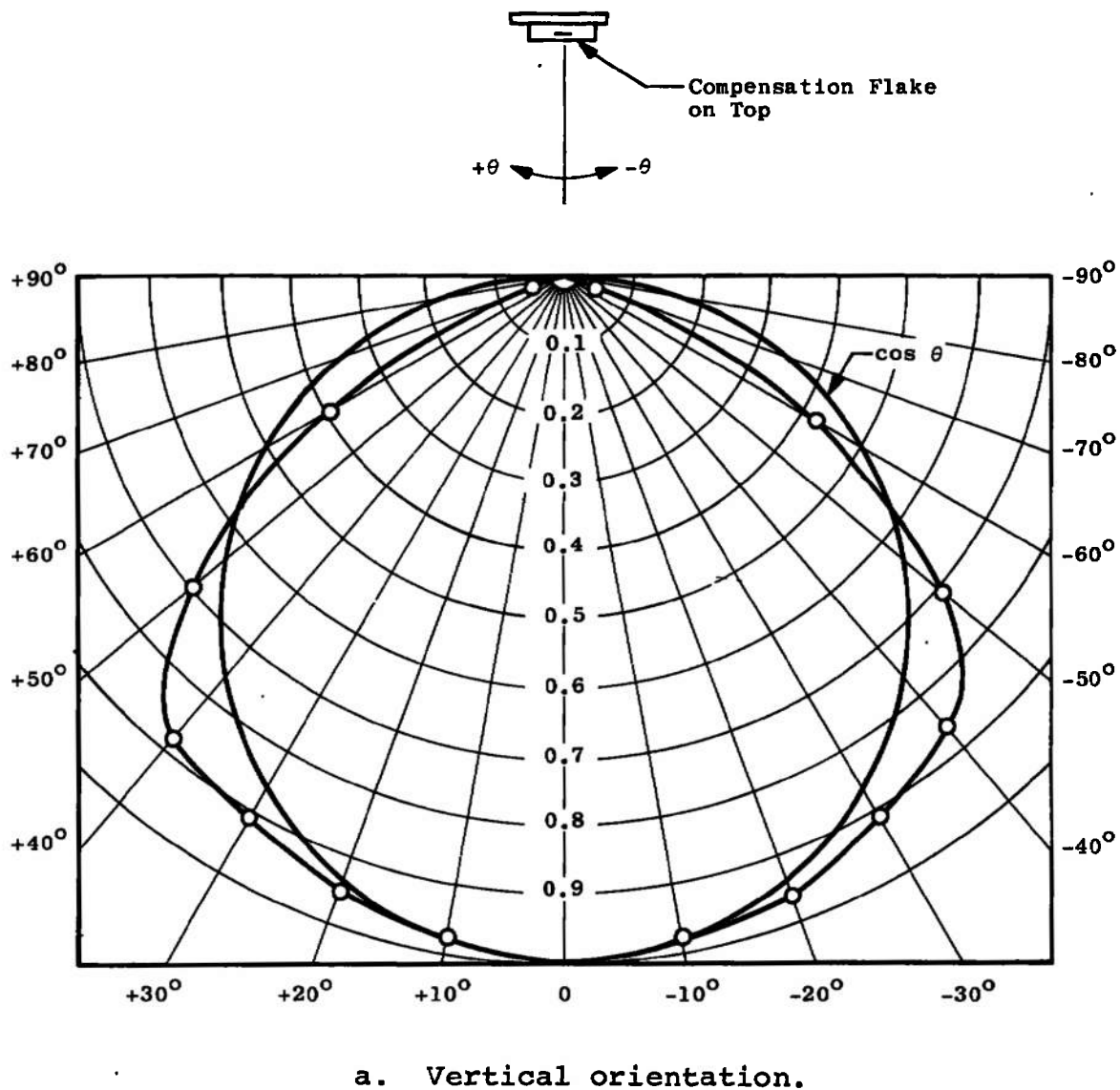
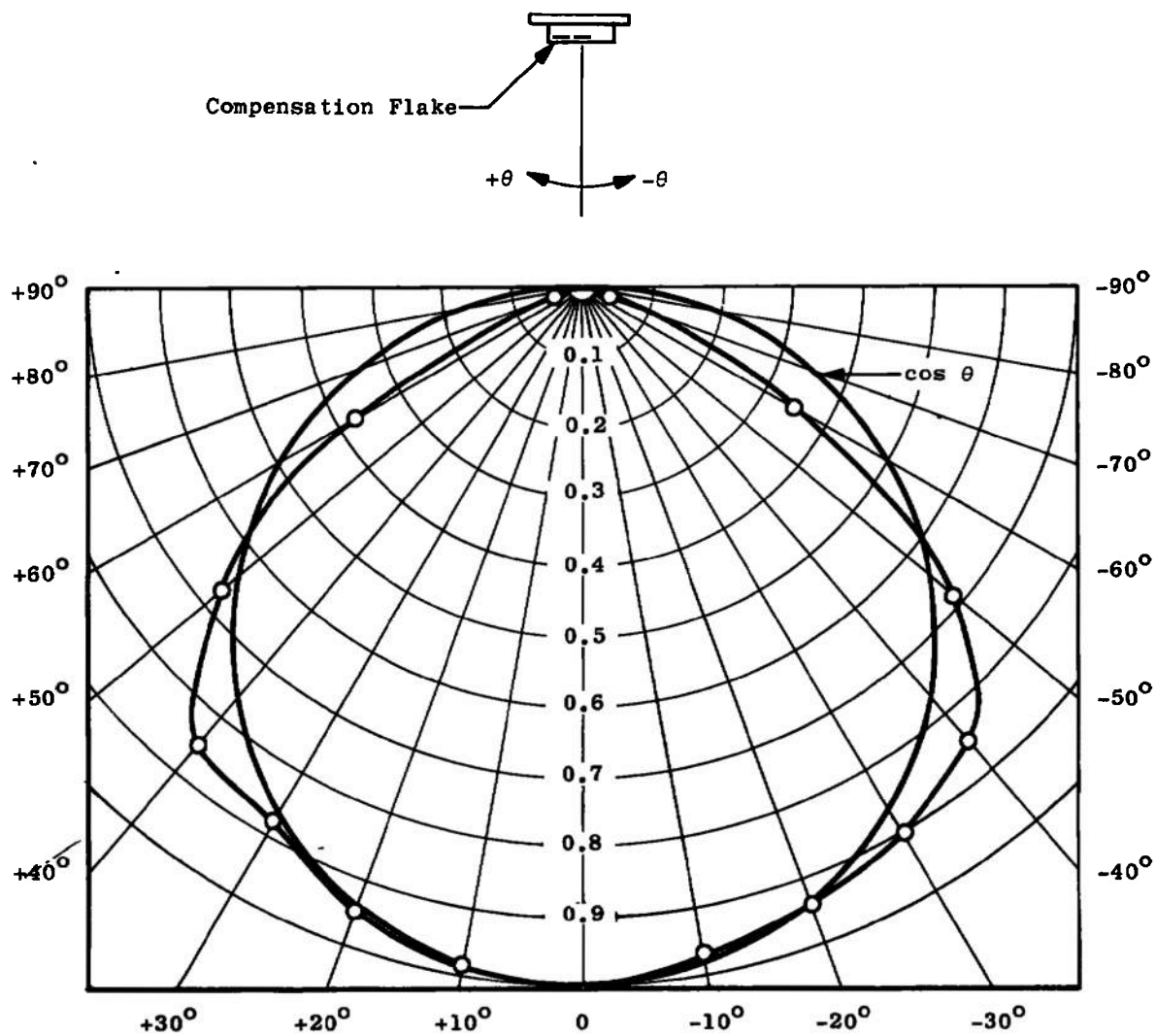


Figure 14. Directional sensitivity of a thermistor detector with flat KRS-5 window.



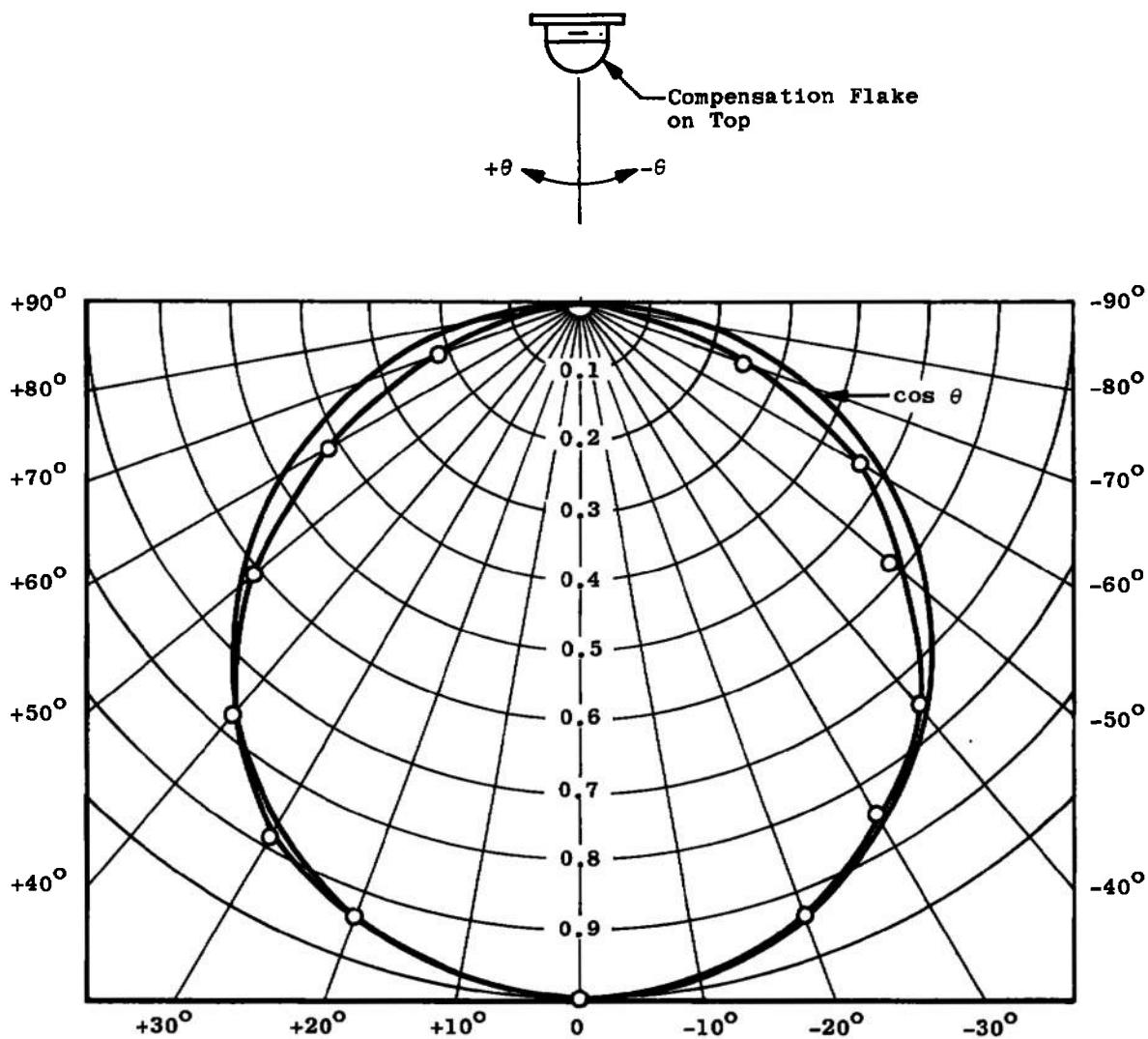
b. Horizontal orientation.

Figure 14. (continued)

for installation on a thermistor detector. This dome is evident in Figure 9, page 26. The directional characteristics of this detector (Figures 15a and 15b) are essentially Lambertian. The variation from  $\cos \theta$  as  $\theta$  approaches 90 degrees is attributed to mechanical blockage of the active flake. The significant variation in the  $-\theta$  direction in Figure 15b is attributed to the fact that the tab over the compensation flake does not completely shield the compensation flake in this direction. This could have been corrected with a slight tab modification.

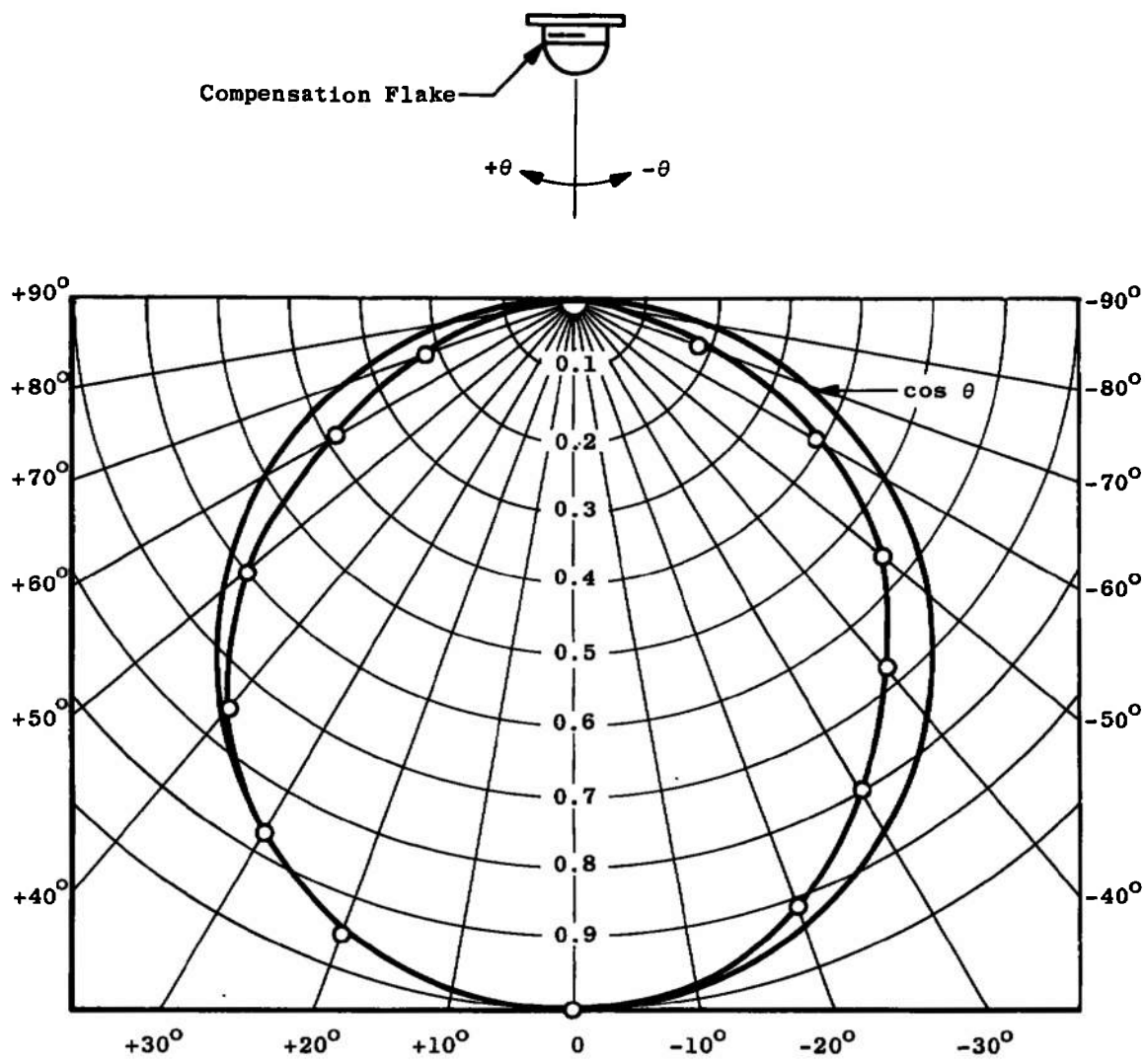
It was assumed that this modified detector approximated a Lambertian detector closely enough for use on the reflectometer.

A third significant problem related to maximizing the hemispherical detector signal-to-noise ratio. When the reflectometer was first assembled the energy was chopped at 13 Hz. The detector signal was contaminated with random noise of magnitude  $\pm 0.5 \mu\text{v}$  up to  $\pm 2 \mu\text{v}$  on some occasions. This was enough noise to render the reflectometer unusable. To resolve the situation the HR-8 amplifier was applied as a tuned frequency voltmeter to analyze the spectral character of the detector noise. The rms noise voltage,  $e_n(f)$ , was measured as a function of frequency from 15 to 150 Hz. These values were squared and divided by the bandwidth,  $\Delta f$ , of the HR-8. The resulting  $[e_n(f)]^2/\Delta f$  values were proportional to the noise power per unit bandwidth at frequency  $f$ . The data were normalized to the 15 Hz value and are plotted



a. Vertical orientation.

Figure 15. Directional sensitivity of a thermistor detector with hemispherical KRS-5 dome.



b. Horizontal orientation.

Figure 15. (continued)

in Figure 16. For comparison, a normalized  $(1/f^{1.5})$  curve is also plotted in Figure 16. These data indicated that the chopper frequency should be increased to reduce the noise. Since the thermistor detector was fast enough to accommodate such an increase, the chopper frequency was changed to 100 Hz. This reduced the noise by a factor of five or six to a level well below 0.1  $\mu\text{v}$ . However, there remains intermittent periods in which the hemispherical detector still produces noise voltages of  $\pm 2$  or 3  $\mu\text{v}$ . All efforts to remedy this problem have failed. The symptoms suggest an intermittently noisy connection within the detector housing.

Another way to improve the detector signal-to-noise ratio is to simply pass more energy into the sphere by increasing the infrared source temperature. Incandescent filaments of carbon, tungsten and a 1/4 inch diameter silicon carbide (Globar) rod were operated in the helium atmosphere. Of these, the Globar gave the most satisfactory results when operated at 650 watts (three times rated power). However, this input power heated the Globar to near the SiC sublimation temperature (2000 °C) and the Globar would last only four to six hours.

An infrared source of the type used by Wood (8) was installed in place of the Globar and was found to produce almost exactly as much infrared energy as the 650 watt Globar. Wood's source consists of a standard 1000 watt, quartz iodine lamp mounted concentrically in a 2 inch O.D. stainless steel tube of the same length as the lamp.

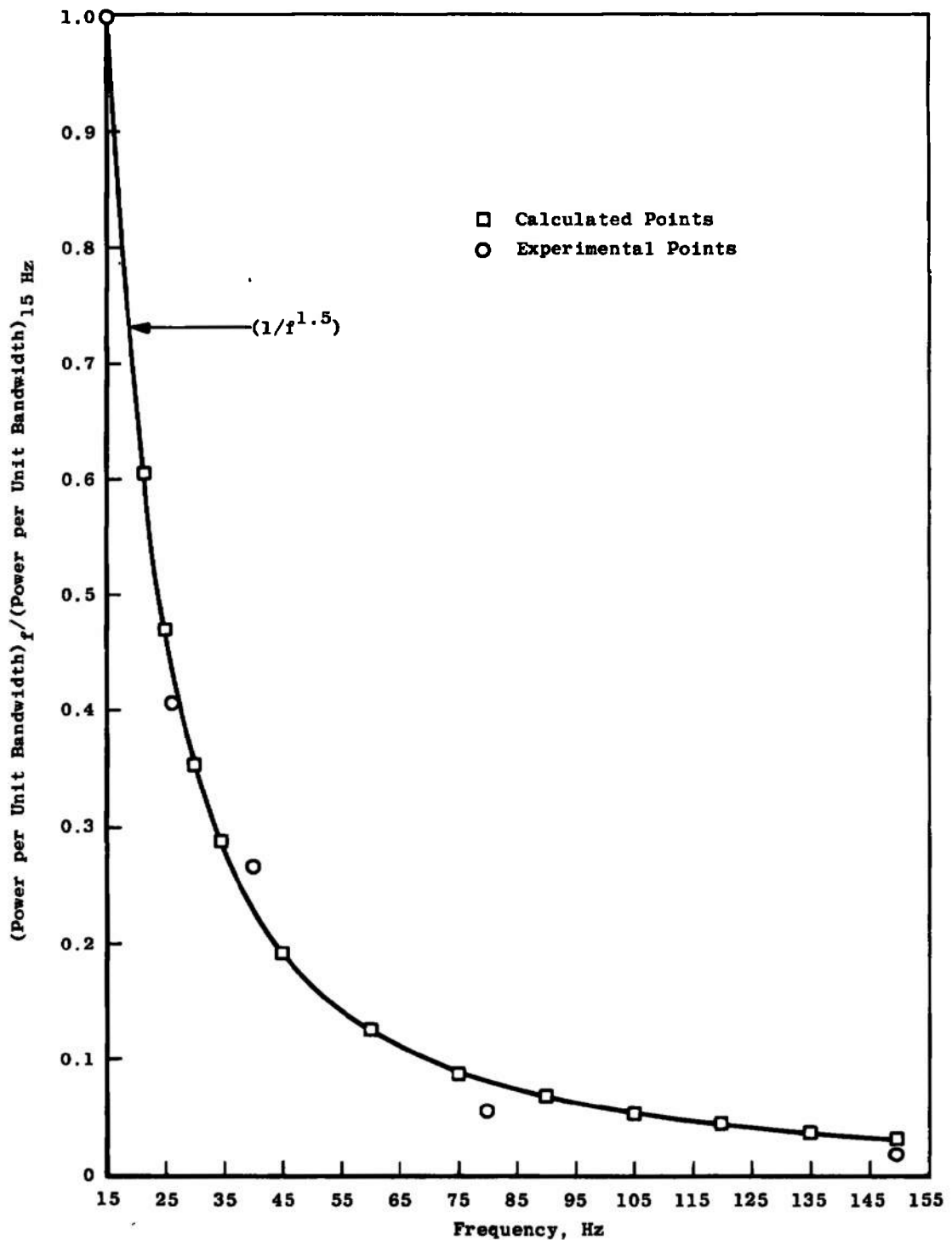


Figure 16. Normalized power density spectrum of the electrical noise from a thermistor infrared detector compared to a  $(1/f^{1.5})$  spectral variation.



The ends of the tube are water-cooled and the monochromator slit is focussed on the quartz envelope through a small hole in the side of the stainless tube. The stainless tube heats to dull red in the middle, and while the temperature of the quartz envelope inside the tube was not measured, it undoubtedly approaches the softening point of quartz (1600 °C). At any rate, this infrared source functions very well and was used in taking all of the experimental reflectance data.

## CHAPTER IV

## EXPERIMENTAL RESULTS

I. SUMMARY AND ANALYSIS OF  
EXPERIMENTAL RESULTS

In Chapter II it was found that the change,  $\Delta E$ , in the hemispherical detector signal when a sample was placed on the sample port divided by the hemispherical detector signal,  $E$ , with no sample on the sample port was closely approximated by Equation 33:

$$\frac{\Delta E}{E} = \frac{\rho_s \rho_w \left( \frac{A}{A_o} \right) \left( \frac{A_s}{A_o} \right)}{[1 - \rho_w (A/A_o)]} \quad (39)$$

The sphere parameters for the reflectometer were established at  $A/A_o = 0.978$  and  $A_s/A_o = 1.09 \cdot 10^{-2}$  and  $\rho_w$ , for a test sample coated at the same time as the sphere interior, was measured to be 0.95. Substituting these values in Equation 39 gives the reflectometer operating equation:

$$\frac{\Delta E}{E} = 0.145 \cdot \rho_s \quad (40)$$

Attempts to experimentally verify Equations 39 and 40 were made in various ways, one of which was to select three samples of varying  $\rho_s$  and to measure  $\Delta E/E$  vs  $\rho_s$  at  $\lambda = 7\mu$ .

The samples consisted of a gold mirror, a diffusely reflecting, sand-blasted aluminum sample and a diffusely reflecting sample of Molykote<sup>®</sup> M-8800 dry lubricant. The spectral, directional-hemispherical reflectances,  $\rho_{\lambda dh}(\theta, \phi)$ , of these samples were determined at  $\theta = 15^\circ$  on the heated cavity reflectometer and found to be 0.98, 0.66 and 0.24 respectively at  $7\mu$ . Also, the directional reflectances were demonstrated to be independent of  $\theta$  up to 70 degrees, which is the instrument limit on  $\theta$ . Therefore, since  $\rho_{\lambda dh}(\theta, \phi)$  was constant,  $\rho_\lambda$  was equal to  $\rho_{\lambda dh}(\theta, \phi)$  as shown by Equation 13, and the samples were usable as "working standards" for verifying Equation 40.

Figure 17 shows the resulting variation of  $\Delta E/E$  vs the bi-hemispherical reflectance with 1.3 mm monochromator slits. A straight calibration line is drawn through the origin and through the gold mirror reflectance value because these are the two most dependable calibration points. The Molykote<sup>®</sup> and aluminum sample data points are 3.3 per cent and 2.6 per cent of full scale higher than the calibration line. This can be explained on the basis of the Fresnel reflection law (1) which shows that the reflectance of any surface approaches unity at grazing incidence (i.e., as  $\theta$  approaches 90 degrees). Therefore the bi-hemispherical reflectances of the Molykote<sup>®</sup> and aluminum samples are actually somewhat larger than the directional-hemispherical reflectance values used in plotting the points on Figure 17. The gold mirror data point should be the most accurate since

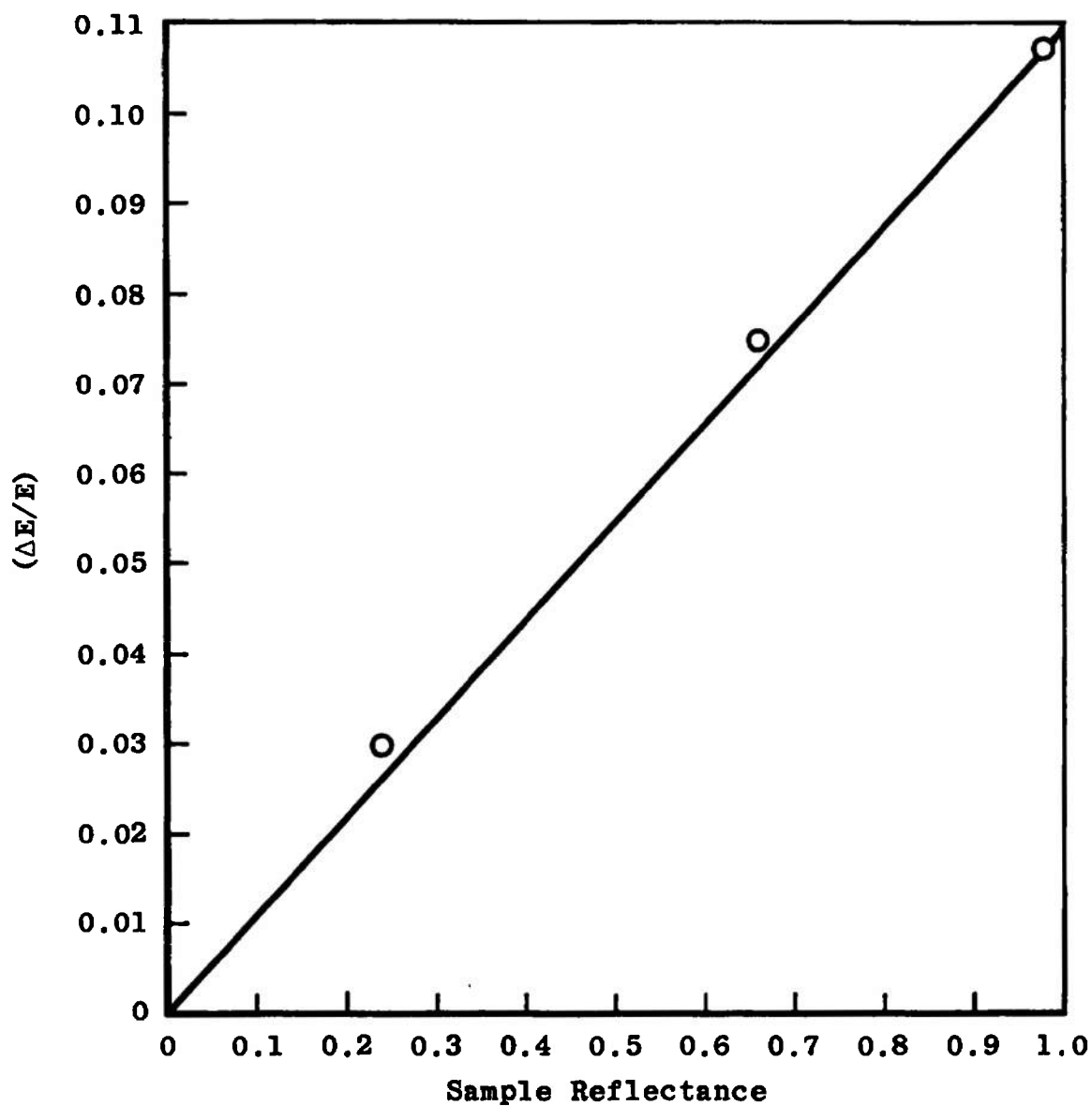


Figure 17. Plot of fractional change in hemispherical detector signal versus bi-hemispherical reflectance at  $7\mu$ .

the gold reflectance in the infrared is near unity (0.98) except at grazing angles where it goes to unity.

The data in Figure 17 do not conclusively show that  $\Delta E/E$  is proportional to  $\rho_s$ , since the reflectances of the working standards are not known accurately enough. However, this linearity was assumed, and gold mirrors were used exclusively in this work as the standards. Their bi-hemispherical reflectance was assumed to be 0.98 on the basis that their measured directional-hemispherical reflectance at  $\theta = 15^\circ$  was 0.98.

According to Figure 17 (the gold standard) the sphere operating equation is:

$$\frac{\Delta E}{E} = 0.109 \rho_s \quad (41)$$

Therefore, the "sphere constant" is 0.109 instead of 0.145 as indicated in Equation 40. This difference is probably due to the sphere wall reflectance,  $\rho_w$ , being less than the 0.95 measured on the test sample. The sphere constant varies sharply with  $\rho_w$ . If  $\rho_w$  is assumed to be 0.93 then the sphere constant calculated from Equation 39 is equal to the experimental value of 0.109. Since the narrow seams between the strips of abrasive paper (see Figure 9, page 26) probably reduce the effective wall reflectance slightly, an experimental sphere constant of 0.109 is considered to be in good agreement with the predicted value of 0.145.

Another test of the reflectometer performance

(Equation 39) is that the sphere constant remain constant for all wavelengths. Using a gold mirror of constant  $\rho_\lambda$  (0.98) to generate the  $\Delta E$  signal, a series of  $\Delta E/E$  measurements were made at various wavelengths with the monochromator slits at 2 mm. The sphere constants were calculated from  $[(\Delta E/E)/0.98]$  at each wavelength and were found to be  $0.105 \pm 0.005$  in the wavelength range from 5.4 to  $16.1\mu$ . Table I presents a summary of these data. The fact that  $\Delta E/E$  is essentially independent of wavelength is another indication that the reflectometer performs as predicted by Equation 39.

A third test of the reflectometer was conducted by determining  $\epsilon_\lambda$  vs  $\lambda$  for the sand-blasted aluminum sample and comparing the results to the normal, spectral emittance  $(\epsilon_\lambda)_n$  as determined with the heated cavity reflectometer. The results are summarized in Table II, and show that the hemispherical to normal emittance ratios generally increase with wavelength. This is the expected result since the sand-blasted surface becomes more specular, and the reflectance increases, at the longer wavelengths.

The final reflectometer performance test consisted of an application of the device to determine the total emittance of fused quartz at 100 °C. This temperature was chosen because published total emittance data on 100 °C quartz are available (9).

This performance test consisted of using the reflectometer to determine the spectral, hemispherical emittance

TABLE I  
EXPERIMENTAL SPHERE CONSTANTS,  $(\Delta E/E)/0.98$ ,  
AT VARIOUS WAVELENGTHS

$\lambda$ ( $\mu$ )	E ( $\mu v$ )	$\Delta E$ ( $\mu v$ )	$\Delta E/E$ For $\rho_{\lambda} = 0.98$	$\frac{\Delta E/E}{0.98}$
5.4	126	13.6	0.108	0.110
7.0	21.9	2.28	0.104	0.106
9.8	8.24	0.82	0.100	0.102
11.1	6.05	0.62	0.102	0.104
12.7	4.31	0.42	0.098	0.100
14.7	2.73	0.28	0.103	0.105
16.1	1.71	0.17	0.100	0.102

TABLE II  
HEMISPHERICAL AND NORMAL SPECTRAL EMITTANCE  
CHARACTERISTICS OF SAND BLASTED ALUMINUM

$\lambda$ ( $\mu$ )	$\rho_\lambda$	$\epsilon_\lambda$	$(\rho_\lambda)_n$	$(\epsilon_\lambda)_n$	$\epsilon_\lambda / (\epsilon_\lambda)_n$
5.4	.63	.37	.63	.37	1.00
7.0	.67	.33	.66	.34	0.97
8.9	.68	.32	.69	.31	1.03
9.8	.70	.30	.70	.30	1.00
11.1	.68	.32	.72	.28	1.14
12.7	.72	.28	.75	.25	1.12
14.7	.73	.27	.76	.24	1.12



of a room temperature quartz plate. The results are shown in Figure 18. Due to detector noise (see following section) the measurements were limited to the region less than  $16\mu$ , and the emittance curve was extrapolated to  $50\mu$  as a straight line. This appeared reasonable both because the emittance curve had leveled out at  $12\mu$  and because the emissive power in the region beyond  $16\mu$  amounted to only 26 per cent of the total emissive power.

The experimental emittance data were used to calculate the total emittance in the exact manner indicated in Equation 5. The calculation was performed graphically as shown in Figure 19. Curve 2 is Planck's function for a  $100^\circ\text{C}$  blackbody. Curve 1 is the product of Curve 2 and the spectral emittance data in Figure 18. The ratio of the area under curve 1 to the area under curve 2 is the total emittance (Equation 5). The areas were measured with a planimeter and ratioed to obtain an  $\epsilon = 0.80$ . This agrees very well with the reported  $\epsilon$  of 0.78 for  $100^\circ\text{C}$  fused quartz (9).

In summary, the results of all the experimental performance tests indicate that the reflectometer functions in the manner defined by the analysis and as specified by Equation 39.

## II. ERROR SOURCES

In the derivation of the reflectometer operating equation (Equation 39) several assumptions are made:

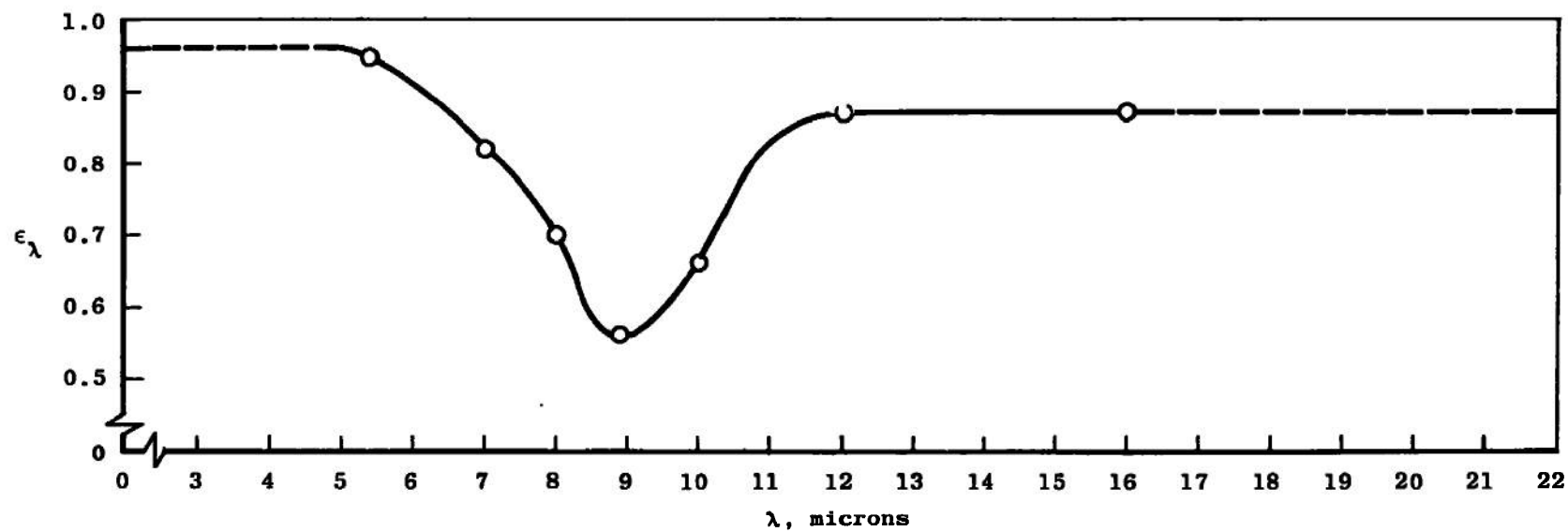


Figure 18. Spectral hemispherical emittance of fused quartz.

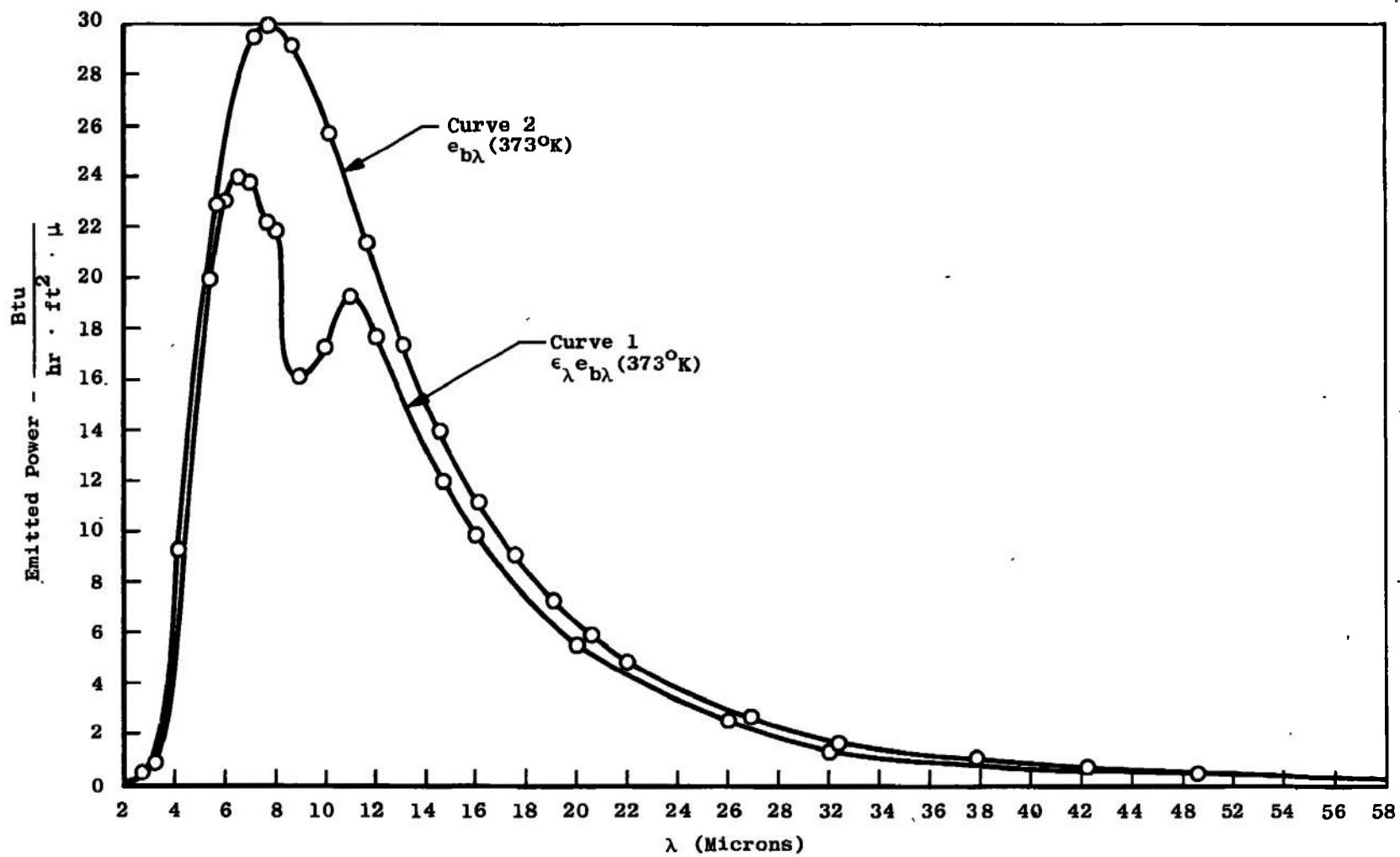


Figure 19. Spectral power emitted from 100 °C fused quartz.

1. The sphere coating is uniform and functions as an ideal diffuse reflector.
2. The hemispherical detector is Lambertian.
3. No infrared energy is absorbed by the gases within the sphere.
4. The baffles and the energy input port do not affect the measurements.
5. A second order term is negligible and can be dropped from Equation 27.
6. A finite sphere wall and coating thickness at the sample port generates no error by incorrectly illuminating the sample at the highest (88 to 90 degrees) grazing angles.
7. Chopped, stray light of incorrect wavelength getting from the monochromator into the sphere produces negligible error.

During the reflectometer design steps were taken to validate each of these assumptions. Those relating to 1 through 3 above were discussed previously. Regarding assumption 4, the baffles were trimmed to minimum size possible.

A brief error analysis of assumption 5 suffices to show that the sample reflectance values calculated from Equation 38 should be corrected by a factor of  $[1.01/(1 + 0.01\rho_s)]$ . Therefore, for low sample reflectance the calculated values are low by 1 per cent of magnitude. For high values the error goes to zero.

To validate assumption 6, to the extent possible, the sphere wall was feathered to a sharp edge around the sample port. However, the sphere coating added to the wall thickness. To reduce stray light the interiors of all transfer optics housings were painted black.

In spite of efforts, there are undoubtedly residual errors associated with each of the above assumptions. However, it is judged that the accumulation of these error sources produces an uncertainty in  $\rho_s$  of no greater than  $\pm 0.01$  (i.e.,  $\pm 1$  per cent of full scale). Another uncertainty of  $\pm 1$  per cent results from the use of the gold mirror as the standard for the reflectometer. Therefore, it is estimated that the reflectometer can produce  $\pm 2$  per cent data at wavelengths where the detector noise does not affect the measurements.

However, the largest error, by far, is due to detector noise. Figure 20 illustrates this point. The top curve shows the variation of the hemispherical detector signal at maximum available energy (2 mm slits). The second, third and fourth curves from the top are the  $\Delta E$  for sample reflectances of 100, 10 and 1 per cent, respectively. The horizontal lines are the observed maximum peak-to-peak voltages of the random detector noise signals for various amplifier output time constants. The noise signals manifest themselves as slow variations in the recorder trace. Figure 11, page 33, illustrates the less significant noise signals which are commonly observed. Under some operating

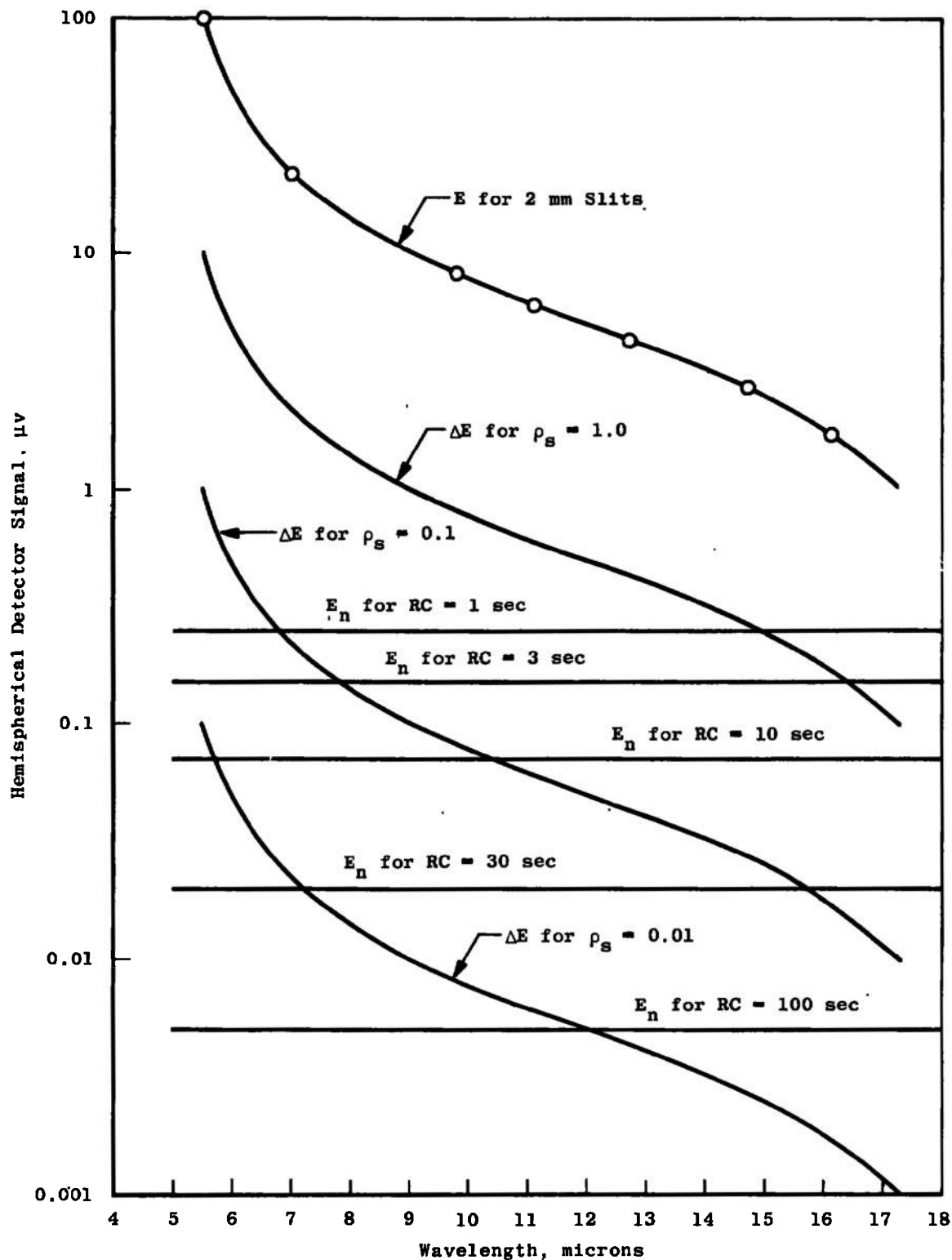


Figure 20. Comparison of detector signal levels to detector noise at various integration times.

conditions the noise can equal or exceed the  $\Delta E$  signal resulting from the sample installation. For example, if the sample reflectance is 10 per cent (third curve in Figure 20) and  $RC = 30$  seconds then  $\Delta E$  is equal to the noise at  $15.7\mu$ , and a reflectance measurement would be impossible. Under these conditions, increasing the time constant to 100 seconds (and consequently increasing the measurement time to 1 hour per reflectance data point) would generate a 4 to 1 signal-to-noise ratio and with graphical noise averaging would allow a reasonably accurate measurement. It is estimated that the reflectance measurement uncertainty at  $16\mu$  (and  $RC = 100$  sec) does not exceed  $\pm 0.10$  (i.e.,  $\pm 10$  per cent of full scale). At shorter wavelengths this uncertainty decreases.

Therefore, in its present state of development, the reflectometer uncertainty is estimated to be less than  $\pm 2$  per cent of full scale at  $5\mu$  and less than  $\pm 10$  per cent at  $16\mu$ .

## CHAPTER V

## CONCLUSIONS

An integrating sphere may be applied to the direct measurement of the spectral, bi-hemispherical reflectance of surfaces in the infrared. This surface property is particularly useful since unity minus this quantity is the spectral hemispherical emittance of the surface. This experimental technique for determining hemispherical emittance was justified both on an analytical basis and to the extent possible with available "working standard surfaces," on an experimental basis. In its present state of development, the experimental reflectometer produces reflectance data with an estimated uncertainty of  $\pm 0.02$  ( $\pm 2$  per cent of full scale) at  $5\mu$ . As a result of excessive detector noise, this increases to  $\pm 0.10$  at  $16\mu$ . Further development work should be directed toward improving the signal-to-noise ratio. This will extend the wavelength range of the instrument and render it a very useful analytical device.



## BIBLIOGRAPHY

1. Sparrow, E. M., and R. D. Cess. Radiation Heat Transfer. Belmont, California: Brooks Cole Publishing Company, 1967.
2. Butler, C. P., and Edward C. Y. Inn. "A Method for Measuring Total Hemispherical Emissivity of Metals," Surface Effects on Spacecraft Materials, First Symposium, Francis J. Clauss, editor. New York: John Wiley and Sons, Inc., 1960. Pp. 195-211.
3. Schmidt, R. N., and J. E. Janssen. "Low-Temperature Total Emittance Calorimeter," Measurement of Thermal Radiation Properties of Solids, Joseph C. Richmond, editor. NASA SP-31. Washington: Government Printing Office, 1963. Pp. 225-230.
4. Dunkle, R. V., et al. "Heated Cavity Reflectometer for Angular Reflectance Measurements," Progress in International Research on Thermophysical and Transport Properties, New York: American Society of Mechanical Engineers, 1962. Pp. 541-562.
5. McNicholas, H. J. "Absolute Methods in Reflectometry," Bureau of Standards Journal of Research, Vol. 1. Washington: Government Printing Office, 1928. Pp. 29-73.
6. Wiebelt, J. A. Engineering Radiation Heat Transfer. New York: Holt, Rinehart and Winston, Inc., 1966.
7. Wolfe, William L., and Fred E. Nichodemus. "Radiation Theory," Handbook of Military Infrared Technology, William L. Wolfe, editor. Washington: Government Printing Office, 1965.
8. Wood, B. E. Private communication. Aerospace Environmental Facility, Arnold Engineering Development Center, Arnold Air Force Station, Tennessee.
9. Gubareff, A. A., J. E. Janssen, and R. H. Torborg. Thermal Radiation Properties Survey. Second edition. Minneapolis: Honeywell Research Center, 1960.
10. Birkebak, R. C. Unpublished classroom, short course notes. The University of Tennessee Space Institute, Tullahoma, Tennessee, May, 1967.

## APPENDIXES

## APPENDIX A

RELATIONSHIP OF DIRECTIONAL EMITTANCE TO  
HEMISPHERICAL EMITTANCE

In the general case of a diffuse, or non-diffuse, infrared emitting surface of differential area  $dA$ , the radiant intensity,  $I_s(\theta, \phi)$ , is defined as the power,  $P_s(\theta, \phi)$ , flowing in the  $(\theta, \phi)$  direction per unit solid angle per unit of emitter area projected normal to the  $(\theta, \phi)$  direction.

That is

$$I_s(\theta, \phi) = \frac{P_s(\theta, \phi)}{dA \cos \theta} \quad (42)$$

The total power emitted by  $dA$  is found by simply integrating over the surrounding hemisphere:

$$P_s = \int_{\Omega} I_s(\theta, \phi) dA \cos \theta d\omega \quad (43)$$

Since  $d\omega = \sin \theta d\theta d\phi$

$$P_s = \int_0^{2\pi} \int_0^{\pi/2} I_s(\theta, \phi) dA \cos \theta \sin \theta d\theta d\phi \quad (44)$$

If the surface is an ideal black surface then the intensity is a constant,  $I_b(0,0)$ , independent of  $\theta$  and  $\phi$ . In this case the total power emitted into the surrounding hemisphere is:

$$P_b = dA \int_0^{2\pi} \int_0^{\pi/2} I_b(0,0) \cos\theta \sin\theta \, d\theta \, d\phi \quad (45)$$

Integrating gives:

$$P_b = \pi dA I_b(0,0) \quad (46)$$

The ratio of Equations 44 and 46 gives the total hemispherical surface emittance,  $\epsilon$ , which is defined as the ratio of the power emitted hemispherically by the surface to the power emitted hemispherically by the ideal black surface:

$$\epsilon = \frac{\int_0^{2\pi} \int_0^{\pi/2} I_s(\theta, \phi) \, dA \cos\theta \sin\theta \, d\theta \, d\phi}{\pi dA I_b(0,0)} \quad (47)$$

Since  $I_b(0,0)$  is a constant it can be taken inside the double integral:

$$\epsilon = \frac{1}{\pi} \int_0^{2\pi} \int_0^{\pi/2} \left( \frac{I_s(\theta, \phi) \, dA \cos\theta}{I_b(0,0) \, dA \cos\theta} \right) \cos\theta \sin\theta \, d\theta \, d\phi \quad (48)$$

The quantity in brackets is the ratio of power per unit solid angle emitted in the  $(\theta, \phi)$  direction by  $dA$  of the real surface to the power per unit solid angle emitted in the  $(\theta, \phi)$  direction by  $dA$  of a black surface. By definition, this ratio is the directional emittance,  $\epsilon(\theta, \phi)$ , of the real surface. Also, since the foregoing definitions deal only with geometrical relations and do not place restrictions on the spectral character of the radiant intensity, it is clear

that Equation 48 is also a valid definition of the monochromatic hemispherical emittance,  $\epsilon_\lambda$ , of the surface.

Therefore:

$$\epsilon_\lambda = \frac{1}{\pi} \int_0^{2\pi} \int_0^{\pi/2} \epsilon_\lambda(\theta, \phi) \cos\theta \sin\theta \, d\theta \, d\phi \quad (49)$$

## APPENDIX B

SHAPE FACTOR FOR ENERGY TRANSFER BETWEEN  
TWO AREAS ON A SPHERICAL SURFACE

A configuration, or shape, factor is defined as the fraction of power incident on one surface, from another surface which is emitting (or reflecting) energy diffusely (6). Consider elemental areas  $dA_1$  and  $dA_2$  in relative positions as shown in Figure 21.

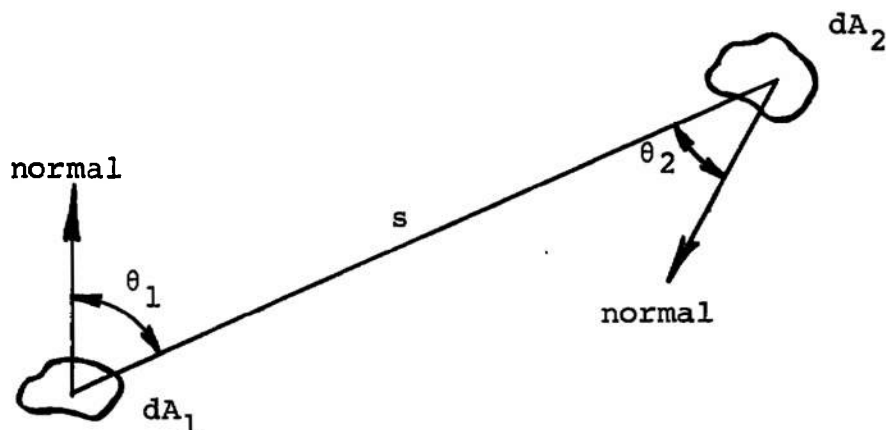


Figure 21. Geometry for shape factor definition.

The magnitude of the shape factor for energy transfer from  $dA_1$  to  $dA_2$  is (6):

$$F_{dA_1 \rightarrow dA_2} = \frac{\cos \theta_1 \cos \theta_2 dA_2}{\pi s^2} \quad (50)$$

If  $dA_1$  and  $dA_2$  are two elemental areas on a sphere (10) then their relative positions are as shown in Figure 22.

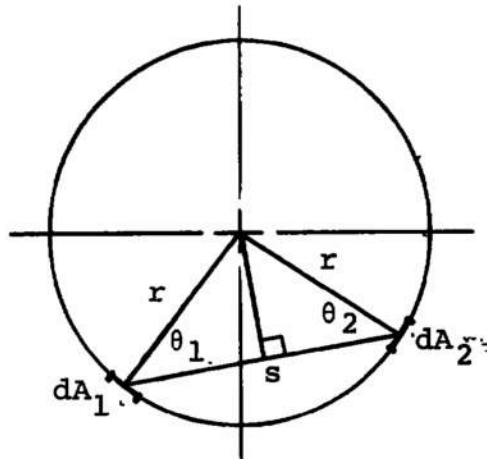


Figure 22. Geometrical relationships when  $dA_1$  and  $dA_2$  are located on a sphere wall.

It is obvious that  $\theta_1 = \theta_2 = \theta$  and  $s = 2r \cos\theta$ .

Therefore, from Equation 50

$$F_{dA_1 \rightarrow dA_2} = \frac{\cos^2\theta \, dA_2}{4\pi r^2 \cos^2\theta} \quad (51)$$

Since  $4\pi r^2 = A_o$ , the area of the sphere, the shape factor is simply:

$$F_{dA_1 \rightarrow dA_2} = \frac{dA_2}{A_o} \quad (52)$$

UNCLASSIFIED


Security Classification

## DOCUMENT CONTROL DATA - R &amp; D

(Security classification of title, body of abstract and indexing annotation must be entered when the overall report is classified)

1. ORIGINATING ACTIVITY (Corporate author) Arnold Engineering Development Center ARO, Inc., Operating Contractor Arnold Air Force Station, Tennessee		2a. REPORT SECURITY CLASSIFICATION UNCLASSIFIED	
		2b. GROUP N/A	
3. REPORT TITLE DETERMINATION OF HEMISPHERICAL EMITTANCE BY MEASUREMENTS OF INFRARED BI-HEMISPHERICAL REFLECTANCE			
4. DESCRIPTIVE NOTES (Type of report and inclusive dates) January 1968 to June 1969- Final Report			
5. AUTHOR(S) (First name, middle initial, last name) Fred G. Sherrell, ARO, Inc.			
6. REPORT DATE November 1969	7a. TOTAL NO. OF PAGES 82	7b. NO. OF REFS 10	
8a. CONTRACT OR GRANT NO. F40600-69-C-0001		9a. ORIGINATOR'S REPORT NUMBER(S) AEDC-TR-69-213	
b. PROJECT NO.			
c. Program Elements 35119F and 35121F		9b. OTHER REPORT NO(S) (Any other numbers that may be assigned this report) N/A	
d.			
10. DISTRIBUTION STATEMENT This document has been approved for public release and sale; its distribution is unlimited.			
11. SUPPLEMENTARY NOTES Available in DDC		12. SPONSORING MILITARY ACTIVITY Arnold Engineering Development Center, Air Force Systems Command Arnold Air Force Station, Tenn. 37389	
13. ABSTRACT A technique for the experimental determination of spectral, hemispherical emittance of surfaces in the infrared wavelength region is suggested. The technique consists of using an infrared integrating sphere to measure spectral, bi-hemispherical reflectance. The feasibility of the technique is justified both on an analytical basis and, to the extent possible, on an experimental basis. A spectral, bi-hemispherical reflectometer is described. The device produces reflectance measurements with an estimated uncertainty of $\pm 2$ per cent of full scale at 5 microns. Due to detector noise the estimated uncertainty increases to $\pm 10$ per cent of full scale at 16 microns. Reflectometer measurements of the spectral hemispherical emittance of fused quartz in the 5 to 16 micron range are presented to illustrate operation of the reflectometer. It is concluded that the device has high potential as an analytical instrument and that developmental efforts should be directed toward extending its wavelength range.			



14. KEY WORDS	LINK A		LINK B		LINK C	
	ROLE	WT	ROLE	WT	ROLE	WT
<p>/ spectral emittance 2 infrared radiation 3 reflectometer 4 reflectance measurement</p> <p> 15-18</p>						